



Study of supramolecular self-assembly of pyridone and dihydropyridone co-crystal: Synthesis, crystal structure, Hirshfeld surface, DFT and molecular docking studies

Lalhruaizela^a, Brilliant N. Marak^a, Dipanta Gogoi^a, Jayanta Dowarah^a, Balkaran S. Sran^b, Zodinpuia Pachuau^a, Ved Prakash Singh^{a,*}

^a Department of Chemistry, School of Physical Sciences, Mizoram University, Aizawl-796004, Mizoram, India

^b Department of Chemistry, Guru Nanak Dev University, Amritsar, Punjab 143005, India

ARTICLE INFO

Article history:

Received 29 November 2020

Revised 25 February 2021

Accepted 25 February 2021

Available online 5 March 2021

Keywords:

Non-covalent interactions

Docking

Intra-molecular

Intermolecular

DFT

Hirshfeld

Crystal

ABSTRACT

Dihydropyridone is synthesized by the multicomponent condensation reactions (MCRs), followed by three different oxidation methods to synthesize pyridone. The 3-D self-assemblies of both the compounds were determined using the single-crystal X-ray diffraction method. Dihydropyridone products are found as a racemic mixture in synthesis and crystallized as co-crystal. Similar structural conformations are observed in both the compounds but stabilized with different non-covalent interactions. Hirshfeld surface analysis is done to analyze the various intermolecular interactions in both the structure. This study gives the clue of driving force in the self-assembly of molecules in crystal lattices. The propensity of inter-molecular contacts to construct the supramolecular assembly was further studied using DFT. The geometrical optimizations of both the compounds were done by the electronic structure method using density functional theory (DFT) to identify the active sites and explore the molecules' chemically reactive parameters. Further, both compounds were docked with Survivin Protein and Kinesin Eg5 protein to analyze the binding affinity with targeted protein.

© 2021 Elsevier B.V. All rights reserved.

Introduction

Dihydropyrimidinones (DHPM's) and their derivatives are heterocyclic compounds synthesized by multicomponent reactions [1,2]. This class of compounds are structural analogs of monastrol became important to the field of medicinal chemistry because monastrol is a very important bio-molecule having many biological activities [3]. Other DHPMs analogs have been synthesized since then, revealing several other pharmacological properties [4]. Monastrol is the protagonist of the DHPMs class. Several studies have revealed that its inhibitory action on human kinesin Eg5 leads to mitotic arrest and, consequently, to apoptosis [5]. At first, this was the main action described for this class of compounds, but some studies have shown other possible targets for these molecules, such as centrin [6], calcium channels [7] and topoisomerase I [8].

2-pyridones are a particular class of compounds with unique pharmacophores that exhibit several biological activities such as analgesic [9], antimalarial [10], antitumoral [11], anti-HIV [12], and

anti-inflammatory [13]. Cyanopyridines are important intermediates for synthesizing many biological important analogs like nicotinamide, nicotinic acid, and isonicotinic acid. 3-cyano-2-pyridone are very significant frameworks in the past few decades. These are the structural basis of the alkaloid ricinine, the first known cyano group-containing alkaloid. Milrinone is also a 3-cyano-2-pyridone derivative used for the treatment of congestive heart failure [14,15]. Some derivative of 3-cyano-2-pyridone has shown anticancer activity [16–18]. 3-cyano-4,6-diaryl-2-pyridone derivatives I and IV (Fig. 1) possess anticancer activity due to their ability to act as survivin inhibitors [19]. Undoubtedly, the need to bridge the gap between minimizing side effects and the mode of action of antimitotic drugs encourage us for further investigations towards the synthesis of the novel potent cytotoxic compound [20,21].

New analogs are designed based on Monastrol kinesin inhibitor and Survivin inhibitor pharmacophore analysis and bio-isoster group application (Fig. 2).

Given the pharmacological importance of 2-pyridone derivatives, the investigations of their structural and electronic properties are fundamental to know the influence of different groups in the molecule to discover the relationship of these groups with their biological properties [22–26].

* Corresponding author.

E-mail address: vedsinghbhu@gmail.com (V.P. Singh).

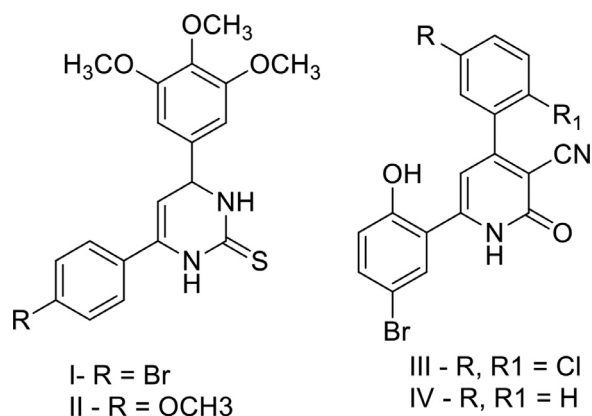


Fig. 1. Cyanopyridones as anticancer agents.

In this study, we report the synthesis of a new molecule containing 2-pyridone and 2-dihydropyridone. Both compounds are fully characterized by IR, ¹H NMR, ¹³C NMR spectrometry, and single-crystal X-ray diffraction (SCXRD). DFT calculations of both molecules carried to study the molecular geometric structure, vibrational frequencies, 1 H & ¹³C NMR chemical shifts, NBO, energies, and molecular electrostatic potential (MEP) using DFT/B3LYP method with 6-311⁺⁺ G(d,p) basis. Also, Hirshfeld surface analyses were performed to analyze molecular packing and surface interactions. *In silico* analysis, it is used to locate small molecules binding affinity in the target protein's active site. In other words, molecular docking investigated the ligand's most stable conformation in the protein's binding package and scored. Therefore, the molecular docking analyses investigated between compounds 3, 4 & 5 and the target protein.

Materials and methods

Synthesis and crystallization

All Chemicals were purchased from Sigma-Aldrich and Merck. Reactions were checked with TLC on pre-coated aluminum sheets of Merck using an appropriate solvent system, and chromatograms were visualized under UV light. For column chromatography, sil-

ica gel (60-120 mesh) was employed, and eluents were ethyl acetate/hexane mixtures. Melting points of all the compounds were recorded on the electrically heated instrument and are uncorrected. The FT-IR spectrum of solid was recorded in reflectance (ATR) mode with Shimadzu IRAffinity-1S spectrophotometer. ¹H and ¹³C NMR spectrums were recorded in CDCl₃ on Bruker AVANCE 300 MHz spectrometer. The chemical shifts are expressed in parts per million (ppm) using tetramethylsilane (TMS) as an internal standard. Mass spectra were done using 6545 QTOF with 1290 Infinity II HPLC equipped with an ESI source. X-ray data of compounds 3, 4 enantiomer co-crystal, and 5 were collected on an Oxford Diffraction Xcalibur CCD and Bruker Axs Smart Apex-1 diffractometer, respectively, at room temperature and processed by SAINT [27]. Lorentz and polarization effects and empirical absorption corrections were applied using SADABS from Bruker [28]. The structure was solved by Intrinsic Phasing methods, using ShelXT [29], and refined by least-squares refinement methods based on F₂, using ShelXL [30]. All non-hydrogen atoms were refined anisotropically. All hydrogen atoms were fixed geometrically with their Uiso values 1.2 times that of the phenylene carbons and 1.5 times that of the methyl group. The hydrogen atoms of the heteroatoms were located from the difference Fourier synthesis and were refined isotropically. All calculations were performed using the Olex2 package [31].

Synthesis of ethyl 6-amino-4-(4-chlorophenyl)-5-cyano-2-methyl-4H-pyran-3-carboxylate

In a 100 mL RB, ethanol (40 mL) was taken and 4-chlorobenzaldehyde (10 mmol) & malononitrile (10 mmol) added and stirred. The mixture ethyl acetoacetate (10 mmol) was added, followed by piperidine (0.2 mL, 2 mmol). The mixture was then stirred at room temperature in an open atmosphere for 10 mins. The precipitate of ethyl 6-amino-4-(4-chlorophenyl)-5-cyano-2-methyl-4H-pyran-3-carboxylate was obtained, which was filtered using vacuum sintered glass funnel and then finally washed with cold methanol.

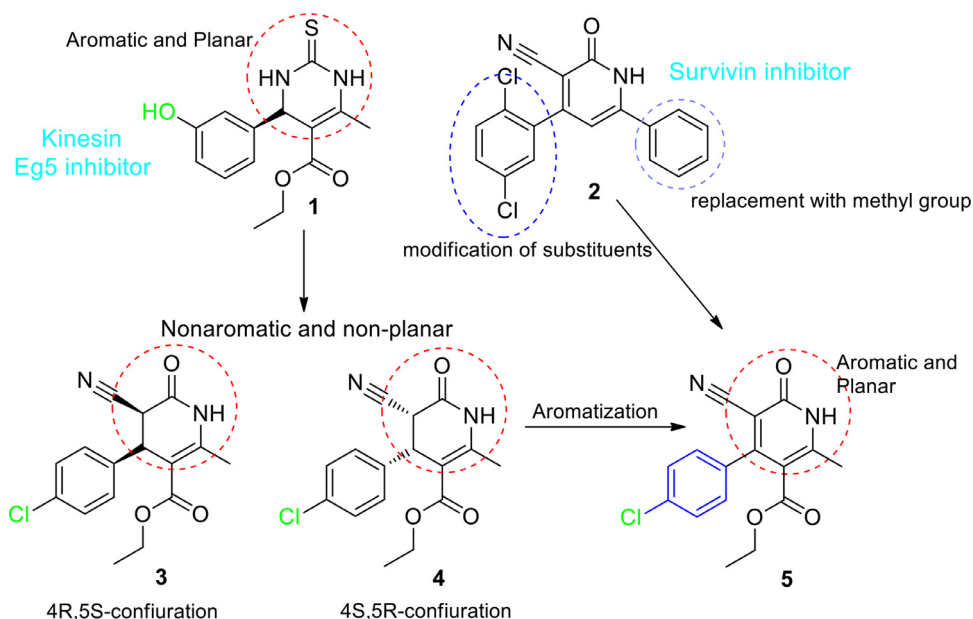
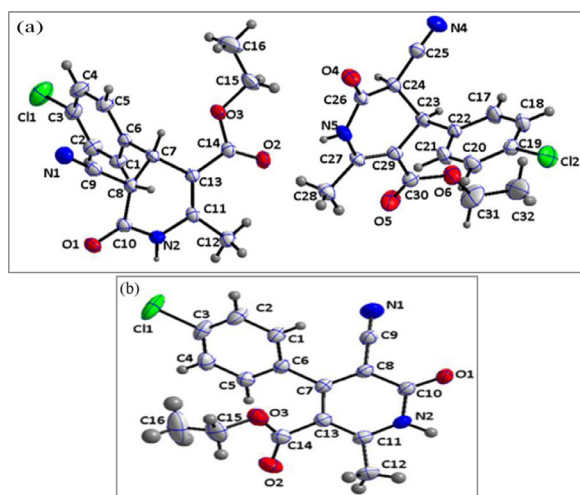


Fig. 2. Kinesin inhibitor (Monastrol 1) & Survivin inhibitor (Compound 2) based designed analog.

Table 1
Crystal data and structure refinement for compound 3 & 4 co-crystal & 5.

Identification code	5 (CCDC 2035459)	3& 4 (co-crystal) (CCDC 2035460)
Empirical formula	C ₁₆ H ₁₃ ClN ₂ O ₃	C ₁₆ H ₁₅ ClN ₂ O ₃
Formula weight	316.73	318.75
Temperature/K	296.15	296.15
Crystal system	Triclinic	triclinic
Space group	P-1	P-1
A, b, c /Å	9.264(5), 9.923(5), 10.327(5)	9.4919(8), 12.9828(11), 14.9912(13)
α /°	64.060(5)	104.030(3)
β /°	73.767(5)	106.305(3)
γ /°	66.810(5)	105.518(3)
Volume/Å ³	778.1(7)	1604.6(2)
Z	2	4
ρ_{calc} /g/cm ³	1.352	1.319
μ /mm ⁻¹	0.259	2.230
F(000)	328.0	664.0
Crystal size/mm ³	0.2 × 0.18 × 0.14 This is not a pattern of 'ccdc' external object linking.	0.23 × 0.18 × 0.15
Radiation	MoK α (λ = 0.71073)	CuK α (λ = 1.54178)
2 θ range for data collection/°	4.424 to 57.932	7.524 to 94.034
Index ranges	-12 ≤ h ≤ 12, -13 ≤ k ≤ 13, -13 ≤ l ≤ 13	-8 ≤ h ≤ 8, -12 ≤ k ≤ 12, -14 ≤ l ≤ 14
Reflections collected	24274	13149
Independent reflections	4048 [R _{int} = 0.0678, R _{sigma} = 0.0512]	2814 [R _{int} = 0.0279, R _{sigma} = 0.0231]
Data/restraints/parameters	4048/0/205	2814/0/409
Goodness-of-fit on F ²	1.057	1.054
Final R indexes [I > 2 σ (I)]	R ₁ = 0.0503, wR ₂ = 0.1223	R ₁ = 0.0378, wR ₂ = 0.0969
Final R indexes [all data]	R ₁ = 0.0873, wR ₂ = 0.1406	R ₁ = 0.0433, wR ₂ = 0.1022
Largest diff. peak/hole / e Å ⁻³	0.21/-0.42	0.20/-0.24

**Fig. 3.** Ortep Diagram of 3 & 4 enantiomeric co-crystal (a) & 5 (b).

Synthesis of ethyl 4-(4-chlorophenyl)-5-cyano-2-methyl-6-oxo-1,4,5,6-tetrahydropyridine-3-carboxylate

To a 2-neck 150 mL RB the synthesized ethyl 6-amino-4-(4-chlorophenyl)-5-cyano-2-methyl-4H-pyran-3-carboxylate (6.7 mmol) was dissolved in ethanol (50 mL) at 80°C. Iodine (10 mol %) was added to the reaction vessel and refluxed using Graham condenser for 2-4 hours monitored by TLC (EtOAc/hexane 3:7). After the reaction was completed, the mixture was concentrated under reduced pressure and then treated with hypo solution (5 mol%) to remove un-reacted iodine. The organic layer was back-extracted with ethyl acetate (twice), usual workup and purification over silica gel column using Hexane: EtOAc (70:30) afforded **3 & 4** enantiomer mixture ethyl 4-(4-chlorophenyl)-5-cyano-2-methyl-6-oxo-1,4,5,6-tetrahydropyridine-3-carboxylate.

Additional technique

The organic layer (ethyl acetate) obtained from the workup process was concentrated in a rotary evaporator by preventing

precipitate formation. The solution was collected in a conical flask, sealed with rubber septa, and then placed inside a freezer (-20 to -25°C) for 2 hours. The precipitate of ethyl 4-(4-chlorophenyl)-5-cyano-2-methyl-6-oxo-1,4,5,6-tetrahydropyridine-3-carboxylate formed (confirmed by TLC), which was collected by filtration. The filtrate that contains the remaining product was subjected to purification by column chromatography. This method facilitates the pure precipitate of the product and reduces the working time and solvent required for purification.

¹H NMR (300 MHz, CDCl₃): δ 1.18 – 1.23 (3H, t, CH₃CH₂-, J = 7.2 Hz); 2.44 (3H, s, CH₃-); 4.08 – 4.17 (3H, m, CH₃CH₂-, CH-); 4.46 – 4.49 (1H, d, CH-, J = 6.9 Hz); 7.18 – 7.20 (2H, d, Ar-H, J = 8.4 Hz); 7.30– 7.33 (2H, d, Ar-H, J = 8.4 Hz); 8.42 (1H, s, -NH-). ¹³C NMR (300 MHz, CDCl₃): δ 14.04 (C, CH₃), 18.91 (C, CH₃), 40.91 (C, CH-Ar), 41.02 (C, CCN), 60.90 (C, CH₂O), 107.35 (C, CCO₂Et), 113.87 (C, CN), 129.18 (C, Ar), 129.21 (C, Ar), 134.36 (C, CCl), 134.44 (C, C-CH), 146.06 (C, CCH₃), 162.89 (C, CO₂Et), 165.16 (C, C=O). IR (KBr): 3263 (NH), 2252 (CN), 1705 (COOR), 1674 (RCONHR), 733 (CCl). HRMS (ESI) (m/z): calculated for C₁₆H₁₅O₃N₂Cl (NH₄) [M+NH₄]⁺ = 336.11095, found 336.11069.

General procedure for the synthesis of ethyl 4-(4-chlorophenyl)-5-cyano-2-methyl-6-oxo-1,6-dihydropyridine-3-carboxylate

Method A (microwave-assisted reaction)

To a solution of ethyl 4-(4-chlorophenyl)-5-cyano-2-methyl-6-oxo-1,4,5,6-tetrahydropyridine-3-carboxylate (3.52 mmol) in ethanol (15 mL), DDQ (3.52 mmol) was added and irradiated in the microwave oven for 2 minutes. The reaction was monitored by TLC (EtOAc/hexane 1:1). After the reaction was completed, ethanol (10 mL) was added to the reaction vessel, which allows for pure crystals of 2-pyridone (which was further collected). The remaining solvents that contain 2-pyridone were collected and purified over silica gel by column chromatography Hexane: EtOAc (1:1).

Method B (thermal assisted reaction)

To a solution of ethyl 4-(4-chlorophenyl)-5-cyano-2-methyl-6-oxo-1,4,5,6-tetrahydropyridine-3-carboxylate (3.52 mmol) in ethanol (15 mL), DDQ (3.52 mmol) was added and heated on

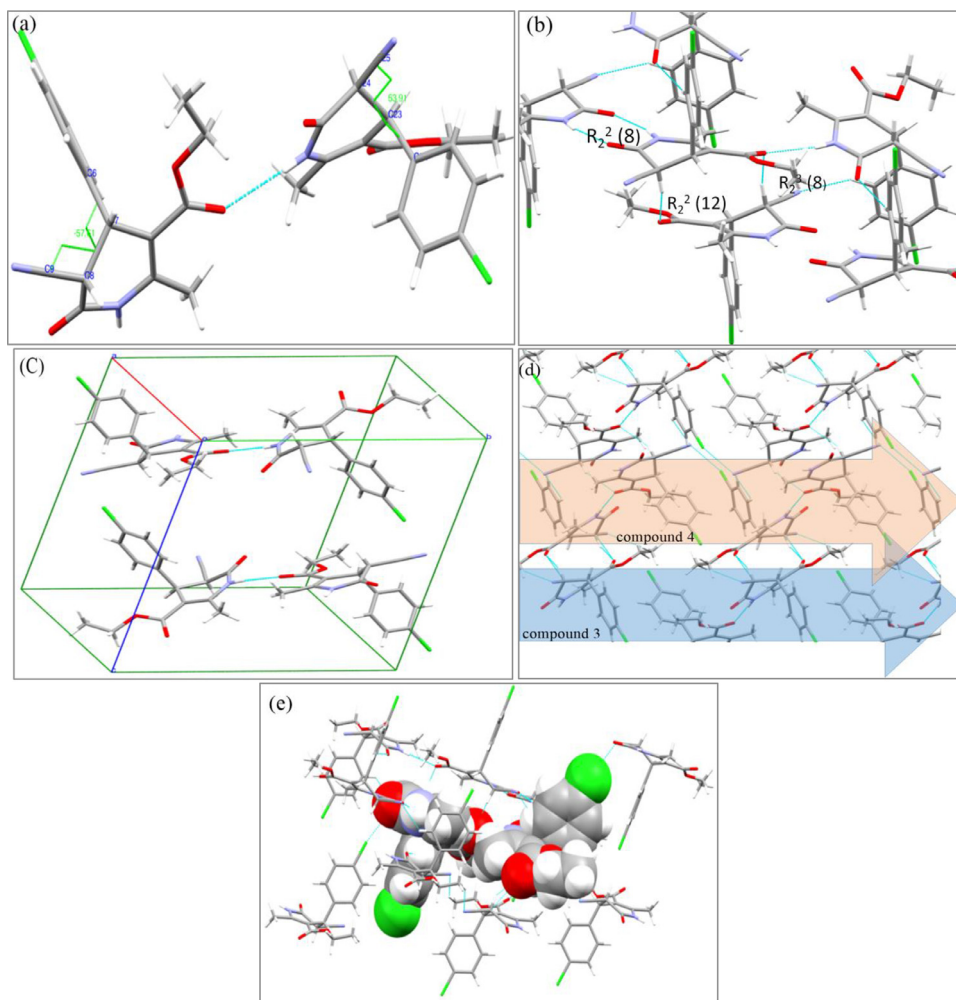


Fig. 4. (a) Hydrogen bonding between enantiomer in crystal packing (b) extended hydrogen bonding network (c) crystal packing in unit cell (d) alternate packing architecture (e) packing pattern of around both enantiomer 3 & 4.

Table 2

Non-covalent interactions (Å) for **3**, **4** & **5** in crystals. Cg is the centroid of the rings

D-H...A	D-H	H...A	D...A	D-H...A	Symmetry Operation
Compound 3 & 4					
N(2)..H(2A)...O(1)	0.783	2.266	3.036	168.27	3-x,1-y,1-z
C(8)..H(8)...O(2)	0.980	2.447	3.307	146.34	3-x,1-y,1-z
N(5)..H(5)...O(2)	0.803	2.245	3.044	173.59	x,y,z
C(21)..H(21)...N(1)	0.930	2.722	3.353	125.85	2-x,1-y,1-z
C(32)..H(32C)...N(4)	0.960	2.700	3.553	148.43	-x,1-y,-z
C(1)-H(1)...O(4)	0.930	2.481	3.294	146.11	1+x,y,z
C(24)-H(24)...O(5)	0.980	2.367	3.211	143.85	1-x,1-y,-z
C(16)- H(16A)...Cg (C1-C6)		3.376			
C(18)- H(18)...Cg (C1-C6)		3.938			
C(12)- H(12C)...Cg (C17-C22)		2.928			
Intramolecular					
C(12)..H(12B)...O(2)	0.960	2.274	2.931	124.85	
C(28)..H(28B)...O(5)	0.960	2.238	2.938	129.05	
Compound 5					
N2-H2...O1	0.961	1.836	2.784	167.99	-x,1-y,-z
C12-H12C...O1	0.960	2.662	3.481	143.48	-x,1-y,-z
C5-H5...O2	0.930	2.385	3.259	156.48	1-x,-y,1-z
C4-H4... Cg(C1-C6)		3.384			
C1-H1... Cg(N2, C7, C8, C10, C11, C13)		2.761			
Intramolecular					
C(12)..H(12A)...O(2)	0.960	2.801	2.920	98.64	
C(12)..H(12B)...O(2)	0.960	2.617	2.920	87.45	

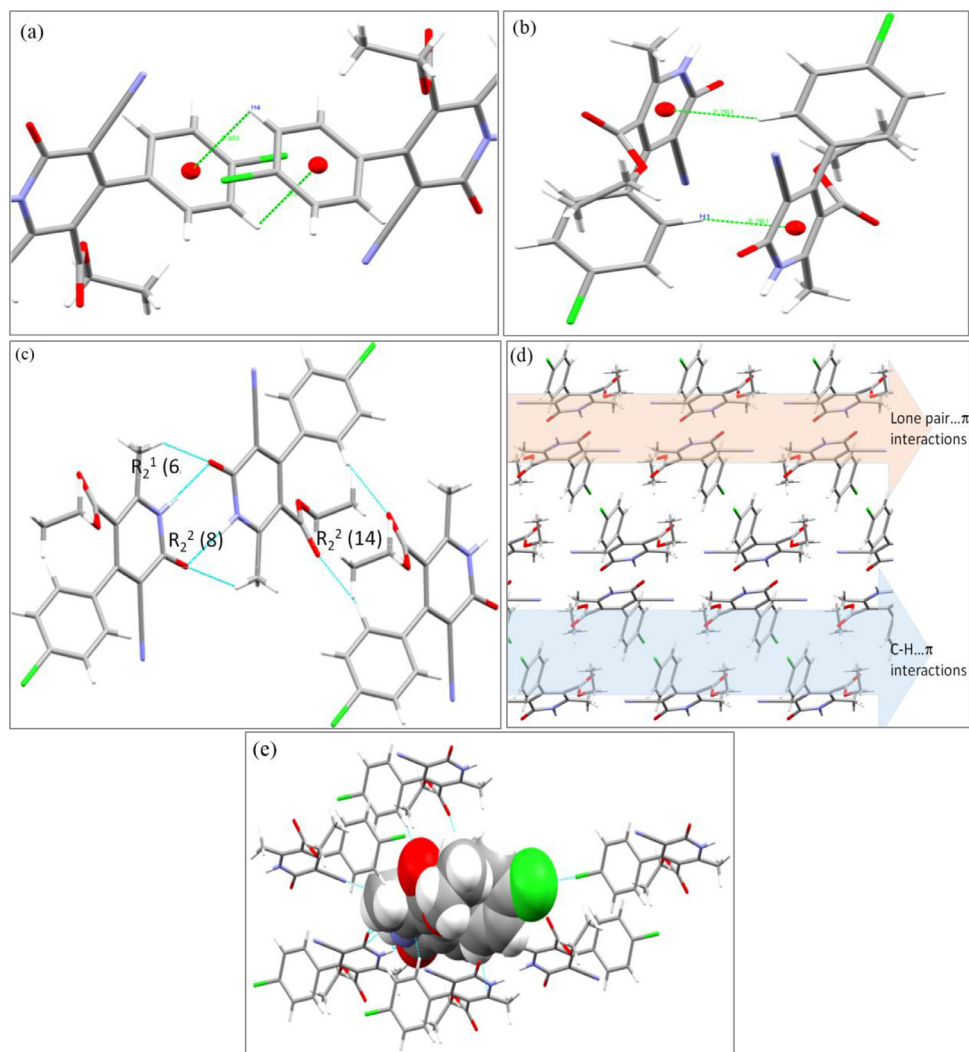


Fig. 5. (a) C-H... π interactions between aryl ring in compound 5 (b) C-H... π interactions in compound 5 between aryl and pyridine ring (c) extended structure of weak interactions (d) alternate packing architecture (e) co-ordination geometry of compound 5 in crystal packing.

Table 3

Calculated total energies (E), dipole moments (μ), and volumes (V) for compounds **3**, **4** & **5** in gas and aqueous solution phases by using the B3LYP/6-311 ++ G ** Method.

Compound no.	Medium	E (Hartree's)	E_{ZPVE} (Hartree's)	μ (D)	V (\AA^3)	V (\AA^3)
3	Gas	-1414.406754	-1414.123156	5.900561	417.925	89.782
3	aqueous solution phases	-1414.428949	-1414.145518	7.860265	328.143	
4	Gas	-1414.406754	-1414.123151	5.899925	417.915	89.77
4	aqueous solution phases	-1414.406754	-1414.145519	5.899925	328.145	
5	Gas	-1413.205588	-1412.944958	7.987571	409.963	86.792
5	aqueous solution phases	-1413.229997	-1412.969646	11.458522	323.171	

a heating mantle at 100° C for 8-10 minutes. The reaction was monitored by TLC (EtOAc/hexane 1:1). After the reaction was completed, ethanol (10 mL) was added to the reaction vessel to form pure crystals of 2-pyridone (which was further collected). The remaining solvents that contain 2-pyridone were collected and purified over silica gel by column chromatography Hexane: EtOAc (1:1).

Method C (auto-oxidation process)

The powdered form of ethyl 4-(4-chlorophenyl)-5-cyano-2-methyl-6-oxo-1,4,5,6-tetrahydropyridine-3-carboxylate was placed on a conical flask and exposed to an open atmosphere at room temperature. It allows the compound to interact with atmospheric

oxygen to undergo self-oxidation from ethyl 4-(4-chlorophenyl)-5-cyano-2-methyl-6-oxo-1,6-dihydropyridine-3-carboxylate, which was monitored by TLC (EtOAc/hexane 1:1). Separation of compounds was done using column chromatography Hexane: EtOAc (1:1). However, this synthetic method was not favored over methods A and B since it was time-consuming as the oxidation process is a surface phenomenon. The resulting yield of the product was low.

Additional technique

Both methods A and B after the reaction of ethyl 4-(4-chlorophenyl)-5-cyano-2-methyl-6-oxo-1,4,5,6-tetrahydropyridine-3-carboxylate with DDQ; ethanol was reduced in a rotary evap-

Table 4

Corrected and uncorrected solvation energies by the total non-electrostatic terms and zero-point vibrational energy (ZPVE) of compounds **3**, **4**, **5** in aqueous solution by using the B3LYP/6-311 ++ G ** Method.

Solvation energy (kJ/mol)			
Condition	$\Delta G_{un} \#$	ΔG_{ne}	ΔG_c
Compound 3	-58.71	10.14	-68.85
Compound 4	-58.73	10.14	-68.87
Compound 5	-64.82	9.36	-74.18

$\Delta G_{un} \#$ = uncorrected solvation energy; ΔG_{ne} = total non-electrostatic terms; ΔG_c = corrected solvation energies.

orator, and methanol (30 mL) was added and was heated to dissolve the product 2-pyridone. The solution was allowed to stand to form pure crystals of ethyl 4-(4-chlorophenyl)-5-cyano-2-methyl-6-oxo-1,6-dihydropyridine-3-carboxylate. Filtered and washed with methanol. The filtrate was collected and concentrated. Crystallization was repeated until the concentration of ethyl 4-(4-chlorophenyl)-5-cyano-2-methyl-6-oxo-1,6-dihydropyridine-3-carboxylate in the filtrate is minimized (confirmed by TLC). The final filtrate was then subjected to purification by column chromatography.

¹H NMR (300 MHz, CDCl₃): δ 0.88 – 0.93 (3H, t, CH₃CH₂-, J = 7.2 Hz); 2.63 (3H, s, CH₃-); 3.93 – 4.0 (2H, q, CH₃CH₂-, J = 7.2 Hz); 7.30 – 7.32 (2H, d, Ar-H, J = 8.4 Hz); 7.46 – 7.49 (2H, d, Ar-H, J = 8.4 Hz); 13.63 (1H, s, -NH). **¹³C NMR** (300 MHz, CDCl₃): δ 13.34 (C, CH₃), 18.89 (C, CH₃), 61.78 (C, CH₂O), 101.50 (C, CCO₂Et), 114.14 (C, CCN), 114.46 (C, CN), 128.70 (C, Ar) 128.94 (C, Ar), 133.68 (C, C-Ar), 136.25 (C, Ar-Cl), 152.66 (C, CCH₃), 159.65 (C, C=O), 162.28 (C, CO₂Et), 164.69 (C, C-Ar). **IR** (KBr): 2245(CN), 1720 (COOR), 1636 (RCONHR), 771 (C-Cl). HRMS (ESI) (m/z): calculated for C₁₆H₁₃O₃N₂Cl (NH₄) [M+NH₄]⁺ = 334.09530, found 334.09500.

Crystal structure determination X-ray Crystallography

Single-crystal X-ray data for compounds **3** & **4** co-crystal and **5** were collected with an Oxford Diffraction Xcalibur CCD and Bruker Axs Smart Apex-1 diffractometer, respectively. Crystallographic details of compounds **3** & **4** co-crystal and **5** are summarized in Table 1.

Computational details

The experimental CIF file structure determined by X-ray crystal data for **3** & **4** co-crystal and **5** were taken as an initial theoretical one. Then, the structure was optimized in the gas phase and aqueous solution with the hybrid B3LYP/6-311++G **method [32,33] and of the Gaussian 16 program [34]. The self-consistent reaction field (SCRF) methodology and universal solvation models were both employed in solution because these schemes consider the solvent effects [35–37]. Molecular electrostatic potential (MEP) [38] and Natural population analysis (NPA) and atomic Merz-Kollman (MK) charges and stabilization energy were predicted in both media with the same level of theory and version 3.1 of the NBO program [39]. The GaussView program was employed to generate the mapped MEP surface of **3** & **4** co-crystal and **5** [40]. The GIAO method was used to predict the ¹H- and ¹³C- NMR spectra of **3** & **4** co-crystal and **5** in aqueous solution by using the hybrid B3LYP/6-311 ++ G **method [41] incorporate in the Gaussian09 program [34]. Also, the frontier orbitals were calculated to predict reactivities of **3** & **4** co-crystal and **5** in both media by using the B3LYP/6-311 ++ G **level of theory. In contrast, the behaviors in both media were evaluated with some descriptors of reactivity such as chemical potential (μ), electronegativity (χ), global hardness (η), global softness (S), global electrophilicity index (ω), and nucleophilicity indexes (E) calculated at the same level of theory [22,24–26,42]. The Hirshfeld surface analysis was performed with Crystal Explorer 3.1 program [43].

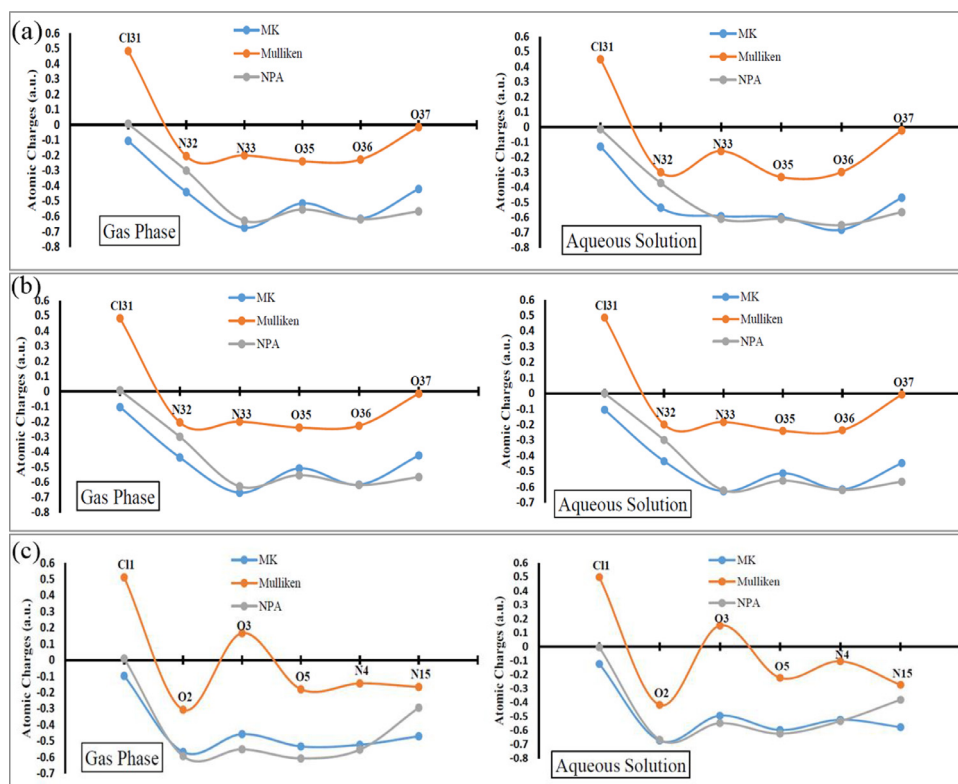


Fig. 6. Atomic MK, Mulliken, and NPA charges of **3** (a), **4** (b), and **5** (c) in the gas phase and aqueous solution by using the B3LYP/6-311++G** method.

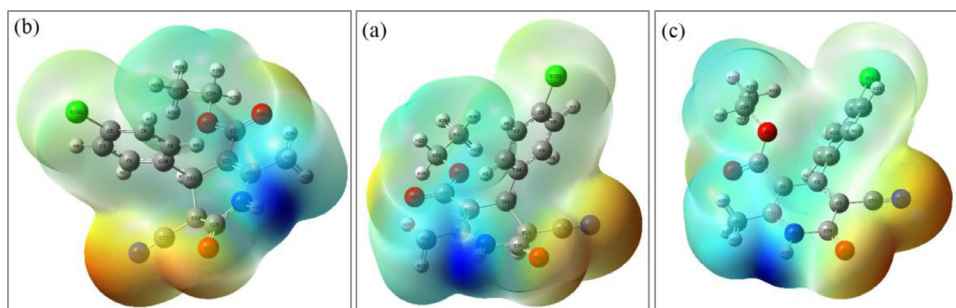


Fig. 7. Calculated electrostatic potential surfaces on the molecular surface of 3 (a) (0.065 a.u.), 4 (b) (0.065 a.u.) and 5 (c) (0.068 a.u.) in gas phase. B3LYP functional and 6-31G* basis set. Isodensity value of 0.005.

Table 5

Comparisons of calculated geometrical parameters of enantiomer **3** in both media with the corresponding experimental ones.

Parameters Bond length (Å)	Gas	Aq	Experimental
C5-C4	1.393	1.394	1.385
C4-C3	1.390	1.390	1.373
C3-C11	1.758	1.764	1.387
C2-C1	1.392	1.393	1.379
C1-C6	1.399	1.399	1.387
C6-C7	1.529	1.529	1.513
C8-C9	1.459	1.458	1.453
C9=N1	1.152	1.152	1.149
C10-N2	1.383	1.370	1.355
C10=O1	1.207	1.216	1.220
C11-C12	1.502	1.500	1.500
C11=C13	1.359	1.359	1.349
C14=O2	1.215	1.219	1.219
C15-C16	1.515	1.514	1.473
C15-O3	1.450	1.454	1.450
Bond angles (°)			
H17,C17,C18	118.817	118.764	119.3
H17,C17,C22	119.811	119.862	119.3
C20,C19,C12	119.527	119.363	120.5
C19,C20,C21	119.207	119.048	119.4
C17,C22,C21	118.195	118.323	117.1
C22,C23,C29	114.039	114.286	114.3
H24,C24,C25	106.900	106.954	106.9
N5,C26,O4	122.389	122.822	123.2
C28,C27,C29	128.053	127.780	127.8
C23,C29,C27	119.672	120.084	120.9
C29,C30,O5	126.976	126.438	127.2
C29,C30,O6	110.975	111.261	110.6
C32,C31,O6	107.613	107.666	108.3
C24,C25,N4	176.709	178.585	177.1
Dihedral angle (°)			
C22,C17,C18,C19	0.166	0.041	0.5
C18,C17,C22,C21	-0.392	-0.492	-1.1
C17,C18,C19,C12	179.720	179.873	-178.9
C21,C22,C23,C29	-33.515	-37.284	-38.3
C22,C23,C29,C30	-84.964	-85.915	-87.0
C23,C24,C26,O4	143.119	143.083	139.7
C28, C27,C29,C23	-177.167	-176.702	-176.1
N5,C27,C29,C30	-179.939	-178.850	179.9
C29,C27,N5,C26	14.142	14.465	14.6
C27,C29,C30,O5	2.581	10.083	20.2
C32,C31,O6,C30	-179.912	179.040	-177.7

In silico analysis of 3, 4 & 5

Molecular docking investigation carried out using the autodockVina [44]. The crystal structures of the survivin and mitotic kinesin Eg5 were retrieved from the RSCB protein data bank (PDB id: 1 × 88 and 3UIH, respectively). The protein preparation was done in chimera [45] by removing co-crystallized ligands, cofactors, and embedded water molecules. It was further processed by adding polar hydrogens and assigning partial charges. The grid parameters for survivin protein were assigned (centered at $x = -26.30$, $y = 1.84$, $z = -19.14$; $31.74 \text{ \AA} \times 25.0 \text{ \AA} \times 23.65 \text{ \AA}$)

Table 6

Comparisons of calculated geometrical parameters of enantiomer **4** in both media with the corresponding experimental ones.

Parameters Bond length (Å)	Gas	Aq	Experimental
C17-C18	1.392	1.393	1.380
C18-C19	1.391	1.390	1.367
C19-C12	1.758	1.764	1.749
C20-C21	1.393	1.394	1.375
C21-C22	1.398	1.399	1.377
C22-C23	1.529	1.529	1.521
C24-C25	1.459	1.458	1.459
C25=N4	1.152	1.152	1.144
C26-N5	1.383	1.370	1.352
C26=O4	1.207	1.216	1.214
C27-C28	1.502	1.500	1.494
C27=C29	1.359	1.359	1.342
C30=O5	1.215	1.219	1.197
C31-C32	1.515	1.514	1.46
C31-O6	1.450	1.454	1.457
Bond angles (°)			
H5,C5,C4	118.548	118.348	119.4
C2,C1,C6	121.231	121.152	121.6
C2,C3,C11	119.566	119.378	119.5
C3,C2,C1	119.088	118.844	120.1
C1,C6,C5	118.194	118.323	117.4
C6,C7,C13	114.043	114.284	113.1
H8,C8,C9	106.899	106.954	106.0
N2,C10,O1	122.388	122.823	123.3
C12,C11,C13	128.054	127.781	128.0
C7,C13,C11	119.671	120.083	119.7
C13,C14,O2	126.975	126.438	127.4
C13,C14,O3	110.972	111.260	110.2
C16,C15,O3	107.611	107.665	106.3
C8,C9,N1	176.714	178.583	177.1
Dihedral angle (°)			
C6,C5,C4,C3	0.205	0.322	0.1
C4,C5,C6,C1	-0.411	-0.634	0.7
C5, C4, C3,C11	179.701	179.735	179.0
C1,C6,C7,C13	-146.961	-143.077	39.8
C6, C7, C13, C14	84.981	85.917	85.3
C7,C8,C10,O1	-143.105	-143.083	-141.7
C12, C11, C13, C7	177.154	176.700	174.9
N2, C11, C13, C14	179.925	178.848	179.4
C13, C11,N2, C10	-14.138	-14.464	-13.3
C11, C13, C14, O2	-2.644	-10.095	-5.2
C16,C15,O3,C14	180.005	-179.062	-174.7

to encompass the dimerization interface and the allosteric site located near to it. Whereas the grid parameters for Eg5 protein were determined based on the native ligand monastrol. The grid is centered on monastrol, making sure all the residues of the binding cavity are encompassed (centered at $x = 18.06$, $y = 24.56$, $z = 49.31$; $18.46 \text{ \AA} \times 21.52 \text{ \AA} \times 21.82 \text{ \AA}$). The exhaustiveness parameter for analyzing the binding affinity was set to 9 modes, and the crystal compounds are subjected to molecular docking with the monomer proteins. The re-docking of crystal compounds confirmed the validation of docking parameters. Further, validation of parameters for Eg5 was done by re-docking of the crystal

Table 7

Comparisons of calculated geometrical parameters of Compound **5** in both media with the corresponding experimental ones.

Bond parameter	Gas	Aq	Experimental
O1=C10	1.216	1.228	1.243
N2-C11	1.355	1.354	1.358
O2=C14	1.212	1.214	1.201
C6-C7	1.491	1.491	1.484
C7=C8	1.386	1.391	1.389
C13=C11	1.386	1.389	1.377
C13-C14	1.495	1.499	1.496
C11-C12	1.503	1.499	1.504
C9=N1	1.156	1.157	1.141
C1-C2	1.391	1.392	1.384
C3-C2	1.392	1.391	1.381
C15-C16	1.518	1.517	1.488
Bond angle (°)			
C14,O3,C15	117.50	117.97	117.4
C11,N2,H2	119.27	118.61	123
C7,C8,C9	122.24	122.23	122.4
C7,C13,C14	123.15	122.57	122.6
O1,C10,N2	119.88	120.29	120.2
N2,C11,C13	118.64	118.73	119.7
N2,C11,C12	115.60	115.70	114.4
C6,C5,C4	120.77	120.60	120.2
O3,C14,C13	112.06	111.97	111.9
O2,C14,C13	123.95	123.62	123.7
C5,C4,C3	119.11	118.99	119.2
C1,C3,C2	119.47	119.26	118.6
C1,C2,C3	119.23	119.02	118.8
O3,C15,C16	112.11	111.95	111.1
Dihedral angle (°)			
C15,O3,C14,O2	-1.76	-0.95	-1.7
C15,O3,C14,C13	-178.19	-178.21	-178.3
C14,O3,C15,C16	-84.68	-85.80	-83.4
H2,N2,C10,O1	-0.23	0.48	2
H2,N2,C10,C8	178.58	179.79	-178
C10,N2,C11,C12	-179.34	179.55	-176.4
C1,C6,C7,C8	-64.20	-66.64	-52.7
C7,C8,C10,O1	-178.75	-179.34	-175.3
C8,C7,C13,C14	174.63	177.83	172.9
C7,C13,C11,N2	2.77	1.64	2.6
C6,C5,C4,C3	-0.72	-0.68	-0.1
C4,C3,C2,C1	0.03	0.28	-0.9

structure of monastrol, which was extracted from Eg5 protein, and then superimposing it with the native monastrol in Eg5 protein. The analysis of docking results was carried out using the pymol and Discovery studio visualizer.

Results and discussion

X-ray crystal structure description

The compound **3** & **4** enantiomeric co-crystal & **5** were analyzed by single-crystal X-ray diffraction (Fig. 3). The summary of crystallographic information is listed in Table 1. The enantiomer **3** & **4** crystallized in the triclinic space group P-1; both enantiomers crystallize in a 1:1 ratio in the crystal lattice unit cell. The compound **5** crystallized in the triclinic space group P-1. The unit cell contains two pairs of enantiomers (4) & (2) molecules, respectively, in both crystals.

The hydrogen-bonding network for enantiomer co-crystal **3** & **4** and crystal packing is in Fig. 4. Enantiomer **3** (RS) and **4** (SR) linked with H (5A)...O (2) hydrogen bonding, whereas pyridone group nitrogen is involved in different types of weak interactions in both enantiomers. Both enantiomers exist as co-crystal in a 1:1 ratio in crystal packing. In addition to intermolecular C-H...O interactions in the extended structure of compound enantiomer **3** & **4** are having intramolecular C-H...O interactions in the compound's flexible arm. This compound, C-H... π interactions, is also exhibited in the crystal packing between the alkyl group and π -electrons of the ring of the adjacent molecule (Table 2). In extensive hydrogen-bonding network terminal carbonyl oxygen, pyridone oxygen & nitrogen of cyano group are involved in three weak interactions and were forming 8, 12 & 8 membered R_2^2 (8), R_2^2 (12) & R_2^3 (8) ring in which C-H...O & C-H...N interactions are involved.

The hydrogen-bonding network for **5** and crystal packing is in Fig. 5. In compound (**5**), pyridone and ester group oxygen molecules are involved in hydrogen bonding, whereas pyridone group nitrogen is not involved in weak interactions. In addition to intermolecular C-H...O interactions compound, **5** are also having intramolecular C-H...O interactions. In this compound, C-H... π interactions are also exhibited in the crystal packing between C-H aromatic and π -electrons of both rings of adjacent molecules (Table 2). In extensive hydrogen-bonding network terminal carbonyl, oxygen & pyridone oxygen are involved in weak interaction and were forming 6, 8 & 14 membered R_2^1 (6), R_2^2 (8) & R_2^2 (14) ring in which C-H...O interactions are involved.

DFT study

Results of optimizations of **3**(RS), **4**(SR) & **5** in the gas phase and aqueous solution using the B3LYP/6-311 ++ G **method

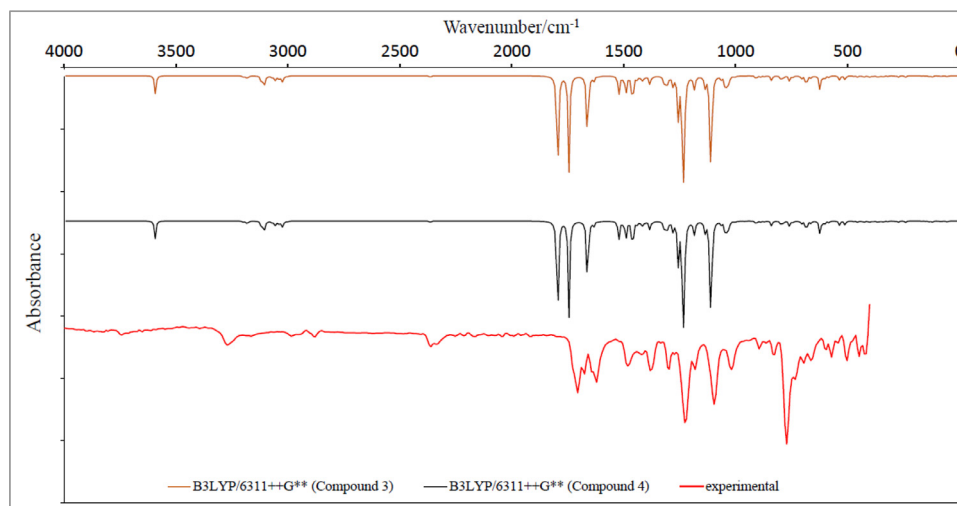


Fig. 8. The experimental infrared spectrum of **3** & **4** compared with the corresponding predicted for the free base using B3LYP/6-311 ++ G **level of theory.

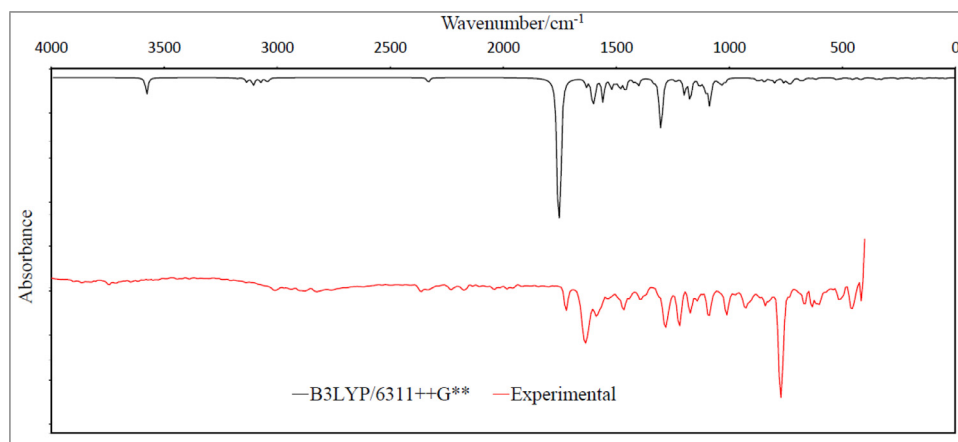


Fig. 9. The experimental infrared spectrum of 5 compared with the corresponding predicted for the free base using B3LYP/6-311 ++ G **level of theory.

can be seen in Table 3, while in Fig. S1 is given the optimized structure together with the atoms labeling. The relative energy value obtained from the difference between the value optimized in solution and the corresponding in the gas phase for both enantiomer **3(RS)** (-0.022362 Hartrees = 58.71 kJ/mol), & **4(SR)** (-0.022368 Hartrees = 58.71 kJ/mol), and **5** (-0.024688 Hartrees = 64.82 kJ/mol). Both enantiomers are found the same relative energy, but compound **5** is having more relative energy in solution. Analyzing Table 3, we observed that the calculated total energies (E) in both media show the most negatives values, as compared with the corrected values by ZPVE energies, while the dipole moment (μ) of enantiomer **3** increases from 5.90 D in the gas phase to 7.86 D in solution, no change in enantiomer **4** and 7.99 D to 11.46 D for compound **5**. Hence, the cationic species of compound **3(RS)** & **5** are probably presented in solution due to the notable increase in the dipole moment value. However, enantiomer **4** (SR) probably exists neutral species in solution due to no change in dipole moment. Simultaneously, a measurable contraction of -89.782 \AA^3 , -89.77 \AA^3 , -86.792 \AA^3 in the volume is observed in solution in all **3(RS)**, **4(SR)** & **5**. Magnitudes and orientations of dipole moment vectors of **3** & **5** in both media are, the directions and orientations practically remain constants in both media. The only change in the magnitudes of μ is observed in solution (Fig. S2). Whereas in enantiomer **4** magnitudes and orientations of dipole moment vectors in both media are, the directions and orientations practically remain constants. The volume contraction observed in solution could be attributed to the hydration of donors (O and N atoms) and accep-

tors groups (N-H, O-H) of H bonds present in the structure of **3**, **4** & **5**. These new H bonds formed in the weak base **3** & **5** could justify the increase of μ and the volume contraction in the solution of **3**, **4** & **5**.

The prediction of solvation energy of **3**, **4** & **5** in an aqueous solution is important, taking into account the presence of donors and acceptors groups in its structure. Hence, corrected and uncorrected solvation energies by total non-electrostatic terms and zero points vibrational energy (ZPVE) of **3**, **4** & **5** by using the B3LYP/6-311 ++ G **method presented in Table 4. Relative energy values of **3**, **4** & **5** are 58.71 kJ/mol, 58.71 kJ/mol, 64.82 kJ/mol, and uncorrected solvation energy value (ΔG_{un}^\ddagger) from Table 4. The results show that the solvation energy value of **5** is slightly higher (most negative) than the enantiomer **3** & **4**, probably because of the aromatic ring in **5**. In contrast, both enantiomers **3** & **4** solvation energy is nearly the same. Besides, both chiral carbons having R, S, and S, R configuration in the enantiomer **3** & **4**. Possibly, the non-aromatic rings limit the hydration of water molecules.

Three atomic charges, molecular electrostatic potentials (MEP), and bond orders expressed as Wiberg indexes are analyzed in the optimized structures of **3**, **4** & **5** in the gas phase and aqueous solution by using B3LYP/6-311 ++ G **level of theory. Thus, atomic Mulliken, Merz-Kollman, and NPA charges and molecular electrostatic potentials (MEP) are summarized in table S1. Here, these properties are presented and analyzed only for the O and N atoms and aromatic rings belonging to donors and acceptors groups of **3**, **4** & **5** in the gas phase and aqueous solution.

Table 8

Observed and calculated wavenumbers (cm^{-1}) and assignments for enantiomers **3&4** in the gas phase using the B3LYP/6-311 ++ G ** method.

Experimental	4R,5S-configuration (compound 3)		Assignments	4S,5R-configuration (compound 4)		Assignments
	Calculated	Intensity (in KM/Mole)		Calculated	Intensity (in KM/Mole)	
3263.56	3592.64	61.2945	ν N2-H2A	3591.61	61.2797	ν N5-H5A
1789.94	1794.80	395.8360	ν O1=C10	1794.79	395.9146	ν O4=C26
1705.07	1744.05	324.1665	ν O2-C14	1744.06	324.0625	ν O5-C30
1674.21	1661.17	256.8311	ν C11=C13	1661.16	256.7104	ν C27=C29
1527.62	1521.70	64.7174	β R ₁ (A1) δ C7-C12	1521.64	64.7211	β R ₁ (A1) δ C23-C28
1257.58	1256.05	140.0662	ν N2-C10 τ wN1-C9 δ C8-H8 δ C7-H7	1256.03	139.8579	ν N5-C26 τ wN4-C25 δ C24-H24 δ C23-H23
1234.44	1236.12	264.8903	δ C8-H8 δ C7-H7 τ wN1-C9	1236.11	266.3348	δ C24-H24 δ C23-H23 τ wN4-C25
1226.73	1229.90	289.9261	δ N2-C10 δ C8-H8 δ C7-H7 δ N2-H2A	1229.89	289.1435	δ N5-C26 δ C24-H24 δ C23-H23 δ N5-H5A
1110.99	1110.79	294.7128	ν O3-C14 ν O3-C15 τ wN1-C9 δ C11C13C7	1110.78	294.5269	ν O6-C30 ν O6-C31 τ wN4-C25 δ C27C29C23
1103.28	1104.04	64.4982	β R ₁ (A1) ν Cl1-C3	1104.00	64.5277	β R ₁ (A1) ν Cl2-C19

Table 9Observed and calculated major wavenumbers (cm⁻¹) and assignments for compound **5** in the gas phase using the B3LYP/6-311 ++ G** method.

Experimental	Calculated	Intensity (in KM/Mole)	Assignments
3579.88	3577.61	84.7997	ν N2-H2
1720.50	1758.57	478.7636	ν O1=C10
1728.21	1748.60	616.9667	ν O2=C14 ν O1=C10
1604.77	1608.11	73.2578	β R ₁ (A1) β R ₂ (A2)
1589.34	1597.34	114.3799	β R ₁ (A1) β R ₂ (A2)
1558.48	1558.70	117.5371	β R ₂ (A2) β N2-H2
1303.87	1303.09	174.9261	β R ₁ (A1) δ C13-C14 β N2-H2
1280.73	1295.88	87.5953	ν C7-C6 ν C12-C11 β N2- H2 τ w N1-C9
1195.86	1198.19	81.8178	γ C15-C16 γ O3-C15 τ w N1-C9
1172.72	1172.78	123.7257	β C1C6C5 τ w C9-N1 γ C15-C16 δ N2-H2
1087.85	1085.61	145.2759	β R ₂ (A2) β C14O3C15 ν C12-C11

Table 10Observed and calculated ¹H chemical shifts (δ in ppm) for enantiomers **3** & **4** in the gas phase and aqueous solution.

4R,5S-configuration (compound 3)			4S,5R-configuration (compound 4)			Experiment
H atom	Gas	Aq	H atom	Gas	Aq	
5-H	7.18	7.22	17-H	7.59	7.54	7.19
4-H	7.49	7.52	18-H	7.58	7.60	7.315
2-H	7.58	7.60	20-H	7.49	7.52	7.315
1-H	7.59	7.54	21-H	7.18	7.22	7.19
2A-H	6.50	6.60	5A-H	6.50	6.60	8.42
7-H	4.51	4.30	23-H	4.51	4.30	4.475
15A-H	3.78	3.83	31A-H	3.99	4.00	4.125
15B-H	3.99	4.00	31B-H	3.78	3.83	4.125
8-H	3.95	3.89	24-H	3.94	3.89	4.125
12A-H	2.03	2.38	28A-H	1.59	1.45	2.44
12B-H	4.46	3.62	28B-H	4.46	3.62	2.44
12C-H	1.59	1.45	28C-H	2.03	2.38	2.44
16A-H	1.06	1.05	32A-H	1.06	1.05	1.215
16B-H	1.26	1.26	32B-H	1.05	1.04	1.215
16C-H	1.05	1.04	32C-H	1.26	1.26	1.215

Table 11Observed and calculated ¹³C chemical shifts (δ in ppm) for enantiomers **3&4** in the gas phase and aqueous solution.

4R,5S Configuration (compound 3)			4S,5R Configuration (compound 4)			Experiment
C atom	Gas	Aq	C atom	Gas	Aq	
14-C	171.48	172.45	30-C	171.47	172.45	162.89
10-C	166.48	167.60	26-C	166.48	167.60	165.16
11-C	158.85	157.95	27-C	158.84	157.95	146.06
3-C	148.33	148.57	19-C	148.33	148.57	134.36
6-C	141.02	141.97	22-C	141.02	141.97	134.44
1-C	132.54	132.67	21-C	137.70	138.04	129.18
2-C	133.72	133.87	20-C	133.76	133.86	129.21
4-C	133.76	133.86	18-C	133.72	133.87	129.21
5-C	137.71	138.04	17-C	132.54	132.67	129.18
9-C	120.29	120.34	25-C	120.29	120.34	113.87
13-C	111.37	112.34	29-C	111.38	112.33	107.35
15-C	64.94	65.52	31-C	64.94	65.52	60.90
7-C	46.53	47.06	23-C	46.53	47.06	40.91
8-C	44.31	44.47	24-C	44.31	44.47	41.02
12-C	17.25	20.02	28-C	17.24	20.02	18.91
16-C	13.49	13.58	32-C	13.48	13.58	14.04

The behavior of three studied atomic charges in the different media is shown in Fig. 6. Regarding this latter figure, we observed in enantiomer **3** & **4** that atomic MK charges on the nine considered atoms present slightly different values and behaviors than those predicted for Mulliken and NPA charges. Both enantiomers **3** & **4** having similar atomic charges to corresponding atoms. On the other hand, the Mulliken charges predict higher values on the chlorine atoms than NPA ones. In comparison, the MK charges predict negative values and where the O21 and N28 atoms present the higher and most negative values.

The three types of charges show that the protonation in aqueous solution could occur only in the nitrogen and oxygen atom be-

cause the three charges show for these atom negative values in both media. On the contrary, the three charges predicted that both oxygen atoms could be protonated in solution.

Molecular electrostatic potentials (MEP) of **3**, **4**, and **5** are evaluated from table S1; different values are observed in both media. The expected tendency is the same, that is, MEP N > MEP O atoms. Particularly, MEP on amide oxygen is > other oxygens while MEP cyano nitrogen presents higher values in the two media than the other ones in compound **3**, **4** & **5**. Nitrogen linked hydrogen is the least values observed in enantiomer **3** & **4**. Hence, these results agree with those observed from the charge's Mulliken Charge, MK, and NPA studies uniform way in both enantiomer **3** & **4**. The

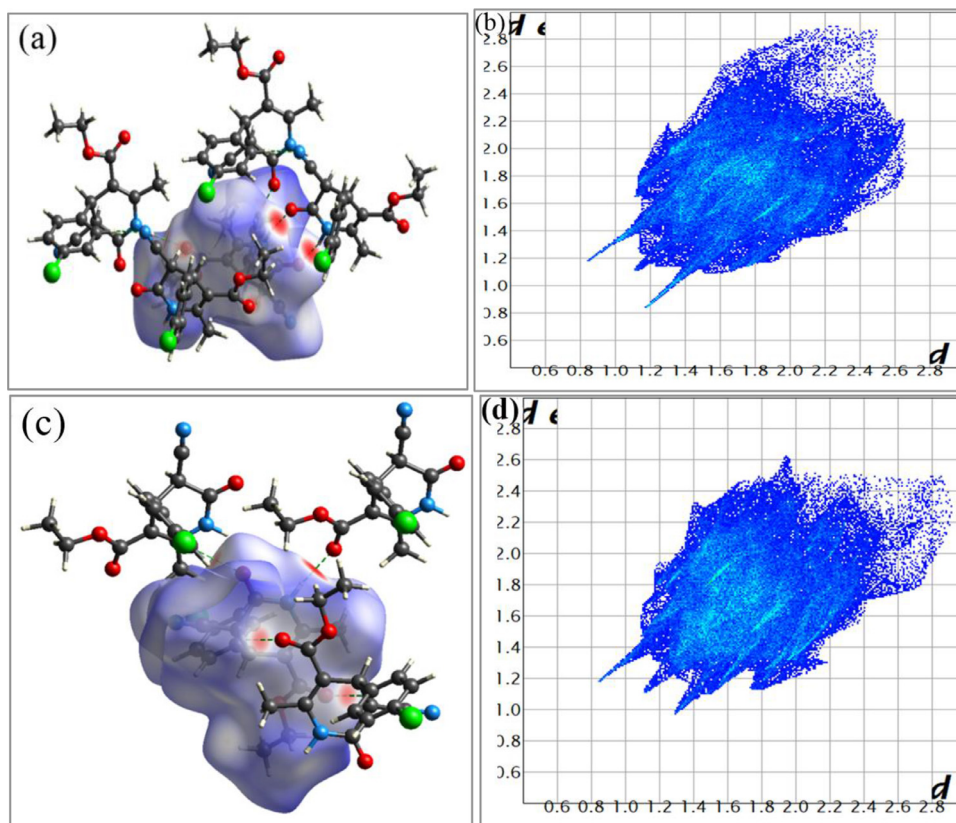


Fig. 10. (a) Hirshfeld surface of enantiomer 3 (b) fingerprint plot of enantiomer 3 (c) Hirshfeld surface of enantiomer 4 (d) fingerprint plot of enantiomer 4.

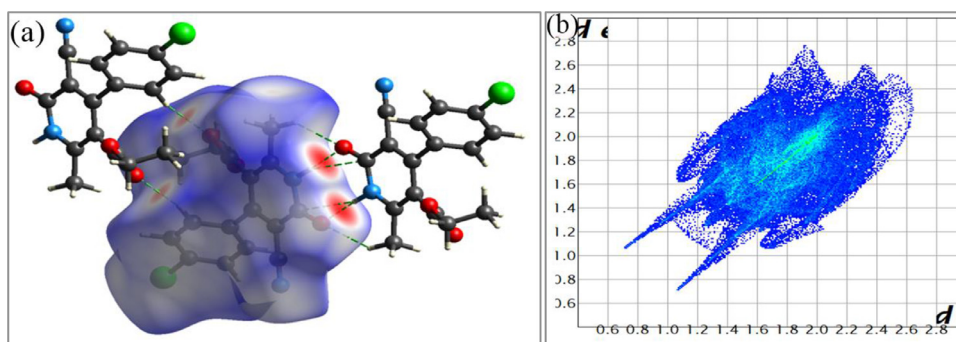


Fig. 11. (a) Hirshfeld surface of enantiomer 5 (b) fingerprint plot of enantiomer 5.

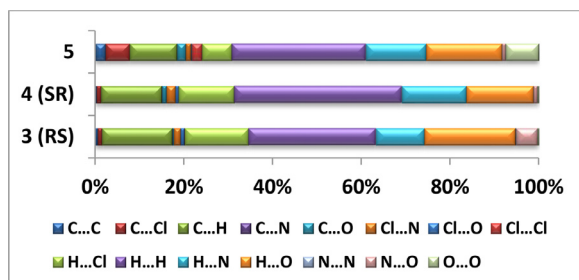


Fig. 12. Percentage contributions in the fingerprint in compounds 3, 4 & 5 are in the bar graph.

mapped MEP surface study is also significant to analyze the main reaction sites where the reaction with potential nucleophiles and electrophiles occurs. This study was performed for **3**, **4** & **5** in the gas phase with the B3LYP/6-31G* method. Fig. 7 presents the calculated electrostatic potential surfaces on all compounds' molecu-

lar surface in both phases with the GaussView program [40]. Analyzing the different colorations on the mapped MEP surface, we observed that the intense red color is located on the amide oxygen and nitrogen of the cyano group and blue color at hydrogen linked with amide nitrogen in compound **3**, **4** & **5**.

Hence, the nucleophilic region is wide, while another less wide site with weak red color is observed on the Oxygen atom. The intense blue color is observed on the N-H bond, revealing the electrophilic sites. Both media results show few changes in the values where the higher ones are observed for the oxygen and nitrogen atoms. Probably, the higher value observed for the nitrogen atom is related to the triple bond with carbon. This result agrees with all compounds in the same way, which means aromaticity could not change the reactive site of **3** & **4** in conversion into compound **5**.

Geometrical parameters

Tables 5, 6 & 7 are summarized the optimized geometrical parameters of **3**, **4** & **5** in the gas phase and aqueous solution by using the B3LYP/6-311 ++ G **method. These parameters are com-

Table 12

Observed and calculated ^1H chemical shifts (δ in ppm) for compound **5** in the gas and aqueous solutions.

H atom	Gas	Aq	Experiment
2-H	8.14	8.23	13.63
2A-H	7.71	7.72	7.475
1-H	7.64	7.58	7.31
4-H	7.54	7.58	7.475
5-H	7.10	7.12	7.31
15A-H	3.40	3.47	3.65
15B-H	4.60	4.63	3.965
12A-H	3.07	2.92	2.63
12B-H	2.50	2.41	2.63
12C-H	1.78	1.81	2.63
16A-H	0.19	0.11	0.905
16B-H	0.66	0.67	0.905
16C-H	1.07	1.00	0.905

pared in the same table with the corresponding experimental ones. The exhaustive analysis shows that better correlations are observed for enantiomer **3** in gas and solvent, around 0.7762 and 0.7685 for bond lengths and of 0.9993 and 0.9991 for bond angle and 0.127 in gas for dihedral angles. The dihedral C17, C18, C19, C12, and N5, C27, C29, C30 angles have signs different from the experimental ones while the other angles present the same signs but values different from the experimental ones. Enantiomer **4** optimized gas and solvent parameters, around 0.9945, and 0.9957 for bond lengths and of 0.9991 and 0.9984 for bond angle and 0.91 insolvent for dihedral angles. The dihedral C4, C5, C6, C1 and C1, C6, C7, C13 angles have signs different from the experimental ones while the other angles present the same signs but values different from the experimental ones. Compound **5** optimized crystal parameters in gas and solvent, around 0.9936 and -0.3234 for bond lengths and of 0.9523 and 0.9418 for bond angle and 0.5923 in gas for dihedral angles. The dihedral H2, N2, C10, C8 angles have signs different from the experimental ones, while the other angles present the same signs but values different from the experimental ones.

Table 13

Observed and calculated ^{13}C chemical shifts (δ in ppm) for compound **5** in the gas phase and aqueous solution.

C atom	Gas	Aq	Experiment
14-C	172.26	172.75	162.28
7-C	170.54	169.34	164.69
11-C	162.95	161.65	152.66
10-C	162.61	163.93	159.65
3-C	149.88	150.10	136.25
6-C	142.91	142.40	136.25
1-C	135.58	135.81	128.70
4-C	134.08	134.13	128.94
2-C	134.01	134.26	128.94
5-C	133.24	132.97	128.70
9-C	120.45	120.74	114.46
13-C	117.31	119.02	101.50
8-C	105.68	105.68	114.14
15-C	65.45	66.52	61.78
12-C	23.53	22.38	18.89
16-C	13.77	13.64	13.34

Here, the differences observed between theoretical and experimental results can be attributed to the calculations because these were performed where the solid-state's packing forces were not considered. These comparisons have demonstrated that despite differences observed in the dihedral angles, both optimized structures using the B3LYP/6-311 ++ G **method can be used to obtain the force fields of **3**, **4** & **5** in both media.

Vibrational study

The experimental FT-IR spectrum of **3**, **4** enantiomers & **5** in the solid-state is in Figs. 8 & 9 compared with the corresponding predicted in the gas phase using the B3LYP/6-311 ++ G **method. An excellent correlation was observed in experimental and calculated spectra of all compounds **3**, **4** & **5**. Some differences were observed due to crystalline packing interactions. For the same reasons, in the higher wavenumber ($4000\text{--}2000\text{ cm}^{-1}$) region, the band attributed to N-H stretching modes is predicted at higher wavenumbers different from the observed in the experimental spectrum.

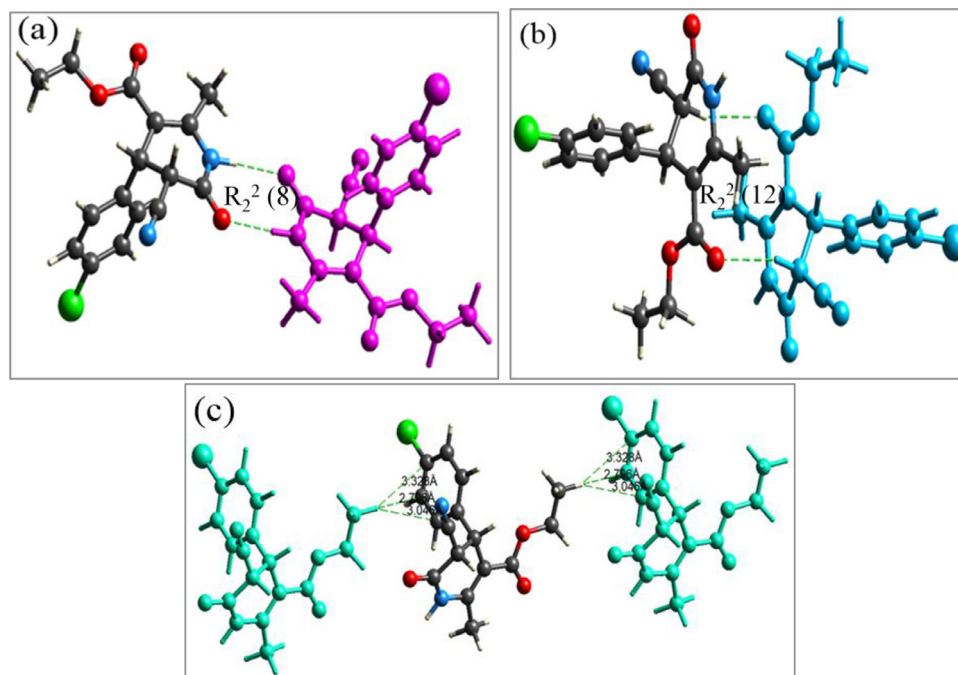


Fig. 13. (a) Non-covalent interactions forming $R_2^2(8)$ (b) Non-covalent interactions forming $R_2^2(12)$ (c) $\text{CH}\cdots\pi$ interactions in weak interactions calculations of enantiomer **3**.

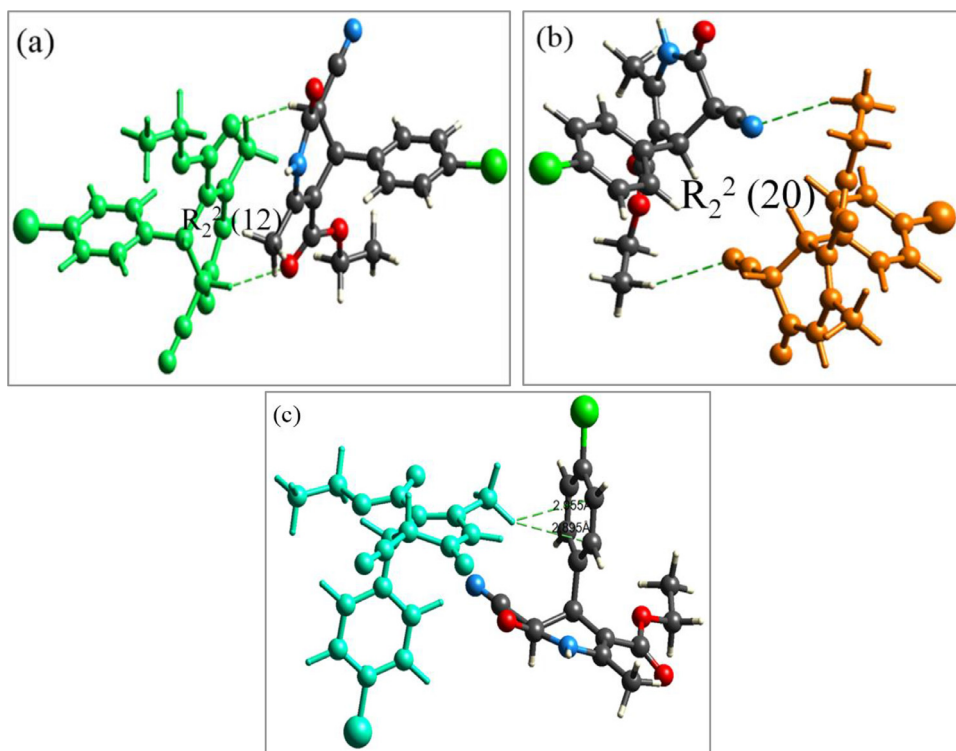


Fig. 14. (a) Non-covalent interactions forming R_2^2 (12) (b) Non-covalent interactions forming R_2^2 (20) (c) CH... π interaction in weak interactions calculations of enantiomer 4.

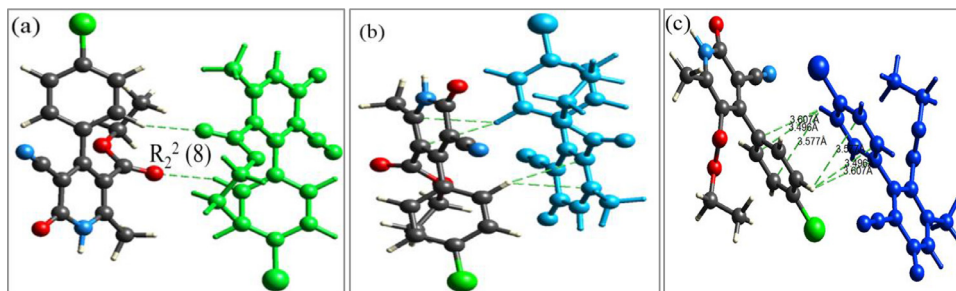


Fig. 15. (a) Non-covalent interactions forming R_2^2 (8) (b) CH... π interactions (c) π ... π interactions in weak interactions calculations of enantiomer 5.

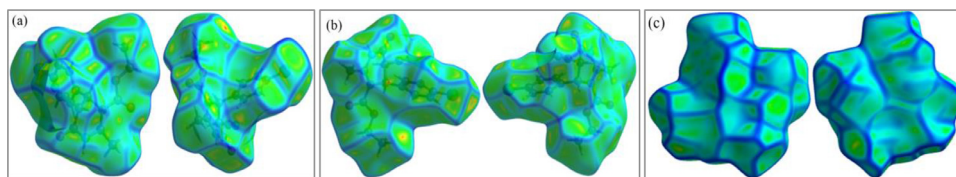


Fig. 16. Curvedness both side view compound 3 (a), 4 (b) & 5 (c).

The predicted spectra in Fig. S3 can be seen as comparisons between the compound's predicted IR spectra using the B3LYP/6-311++G**level of theory. The N33-H34, O35=C16, C17=C22, O37-C23, O37-C24, and C131-C5 stretching modes are predicted with higher intensities in the infrared spectrum in enantiomer 3 & 4 in an experimental and calculated value. Compound 5 stretching modes with high intensity in the experiment is observed for N4-H35, O2=C10, C8-C6, O5=C18, O2=C10, C24-C11, and C24-C11 with good agreement with the calculated value.

According to the total number of atoms (37) present in the structure of enantiomer 3 and 4 total 105 vibration modes are expected. All of them present activity in both spectra because the structures were optimized with symmetries C1. Compound 5 total

numbers of atoms (35) present in the structure and 99 vibration modes are expected, and all of them present in both spectra. Only Potential energy distribution contributions (PED) $\geq 10\%$ were considered in the assignments of vibration modes. Only high intensities observed and calculated wavenumbers and assignments for compounds 3, 4 & 5 in the gas phase using the B3LYP/6-311++G**method are in Tables 8 & 9. The whole table is in supplementary table S2 & S3.

NMR studies

The experimental ^1H and ^{13}C NMR spectra of 3, 4 & 5 were obtained using TMS as an internal standard and CDCl_3 as solvent. On the other hand, the predicted ^1H and ^{13}C -chemical shifts

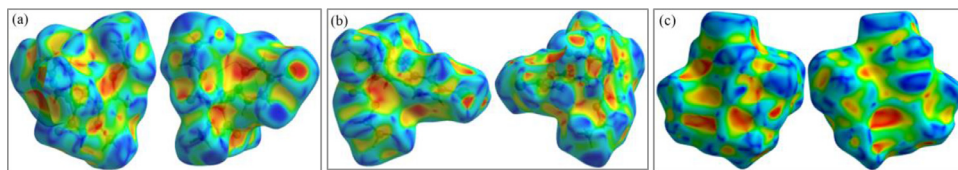


Fig. 17. Shape index both side view of compound 3 (a), 4 (b) & 5 (c).

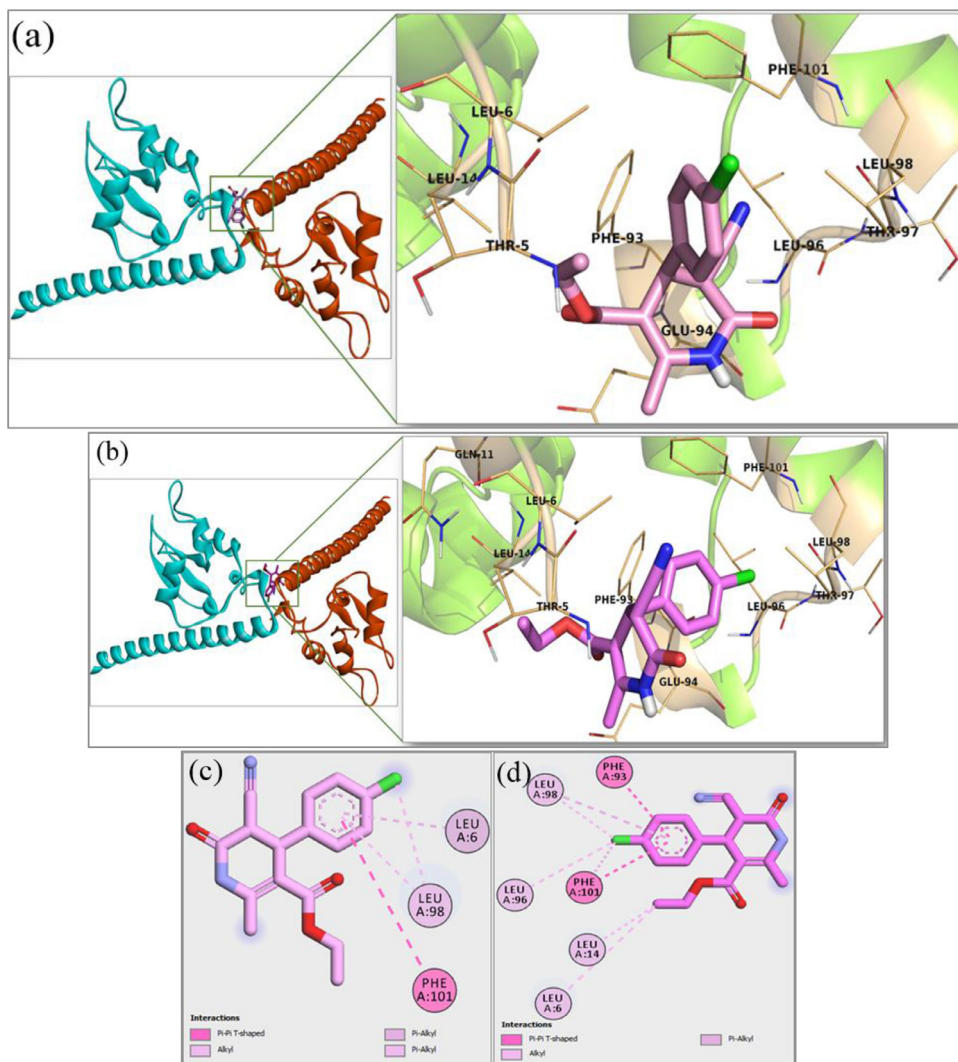


Fig. 18. a) Binding mode of compound 3 at the dimerization surface of survivin protein. b) Binding mode of compound 4 at the dimerization surface of survivin protein. c) 2D representation of the interactions of compound 3 with survivin protein. d) 2D representation of the interactions of compound 4 with survivin protein.

Table 14

Binding energy and the residues involved in the interaction with survivin and kinesin Eg5 protein.

Survivin Protein. Compounds	Docking score	Residues involved in H-bond	Residues involved in other interactions (π -anion, π - σ , π - π , π -alkyl, and alkyl)
3	-6.0	-	Phe101, Leu6, Leu98
4	-6.1	-	Phe101, Phe93, Leu98, Leu96, Leu6, Leu14
5	-6.7	Glu40	Glu40, Lys90, Ile74, Leu87
2 (Survivin inhibitor)	-7.8	-	Leu87, Ile74, Glu40, Lys90, Ala41
Kinesin Eg5 protein			
3	-7.6	Glu117	Glu116, Phe239, Leu214, Ala218, Ile136, Leu160, Tyr211
4	-7.8	-	Glu116, Phe239, Leu214, Ile136, Pro137, Arg119
5	-6.8	Trp127 (halogen bond)	Glu116, Ala218, Pro137, Ala133
1 (Monastrol)	-7.8	Arg119, Glu116, Glu118	Ala218, Leu214, Arg119, Ala133, Pro137

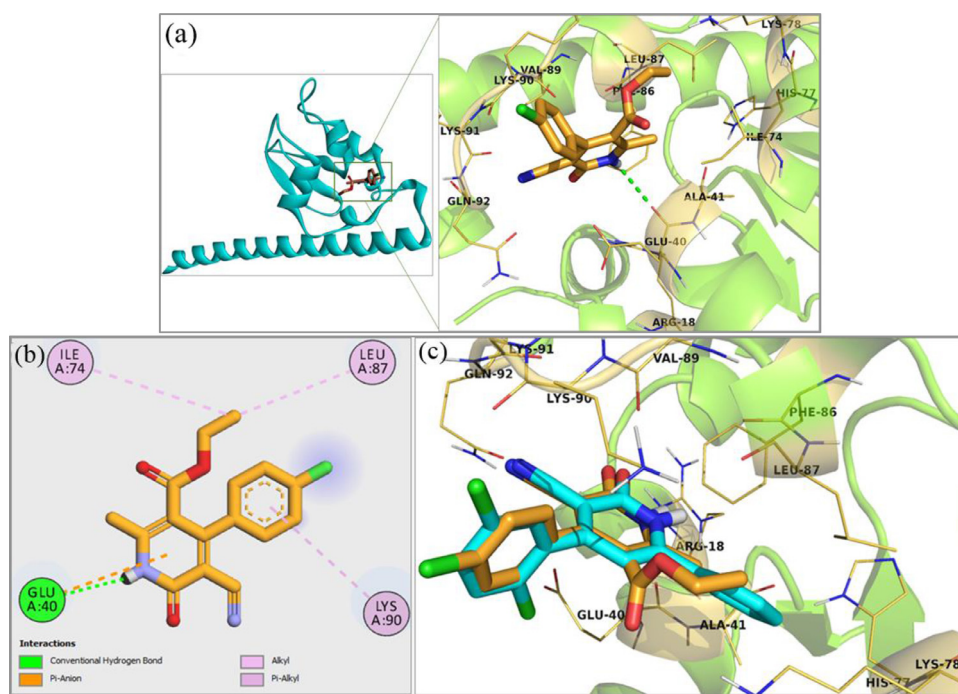


Fig. 19. a) Binding mode of compound 5 at the allosteric site near the dimerization interface of survivin protein. b) 2D representation of the interactions of compound 5 with survivin protein. c) Overlay of compounds 5 (orange) and 2 (reference compound; blue).

for **3**, **4** & **5** in the gas phase and aqueous solution by using the GIAO/B3LYP/6-311 ++ G** method and experimental chemical shift are in tables 10, 11, 12 & 13 [36]. Excellent correlations are observed for the H atoms (0.9670 and 0.9163) and the C atoms (0.99823 & 0.99358) in the solution for enantiomer **3** & **4** respectively. However, for compound **5**, correlations for gas and solution are nearly the same, and all correlations values are >0.9.

Hirshfeld Surface analysis

The 2D fingerprint plots represent the weak intermolecular interactions with the pair of contacts and their percentage of contribution towards the 3D Hirshfeld surface formation. The di and de in the fingerprint plots represent the distance between the nearest internal and external elements to the 3D molecular Hirshfeld surface, respectively [46]. Hirshfeld and fingerprint plots [47] for **3**, **4** & **5** are in Figs. 8 & 9. Both enantiomers **3** & **4** Hirshfeld surface and fingerprint plot found good difference as observed in DFT calculations. The yellowish-red bin on the fingerprint plots is absent in both enantiomers **3** & **4**, which means the absence of weak $\pi-\pi$ stacking in the crystal structure (Figs. 10b & 10d). The spoke-like pattern in the fingerprint plots of enantiomer **3** represents the C-H...O interactions in the crystal lattice in the region of di + de = 2.00–2.9Å (Fig. 10b), whereas in enantiomer **4**, this C-H...O interactions region of di + de = 2.30–2.70Å. The C-H...N interactions in enantiomer **3** can be seen as a pair of unique blue-colored wings in the region of di + de = 3.2–3.6Å (Fig. 10b), and this interaction observed in enantiomer **4** in the region of di + de = 3.2–3.5Å. The C-H...N pair of contacts is also reflected as two characteristic wings occupied in the di + de = 3.2–3.4 Å in enantiomer **3** and the 3.1–3.4 Å in enantiomer **4**, respectively.

The red bin on the fingerprint plots provided information about the presence of weak $\pi-\pi$ stacking in the crystal structure of compound **5** (Fig. 11b). The spoke-like pattern in the fingerprint plots represents the C-H...O interactions in the crystal lattice in the region of di + de = 1.80–2.8Å (Fig. 11B). The C-H...N interactions can be seen as a pair of unique blue colored wings in the region

of di + de = 2.75–3.2Å (Fig. 11b). The C-H...N pair of contacts also reflected as two characteristic wings occupied in the region of di + de = 2.75–3.4 Å (Fig. 11b).

Hirshfeld surface view exactly explained the pattern of molecule conformation exists in the solid-state. Electronic distribution within the compound also explained the existence of non-covalent interactions (Figs. 10 & 11). The surface coverage for both enantiomers **3** & **4** shows a good difference (Fig. 12), taking part in weak interactions. Enantiomer **3** is H...H 30.0 %, Cl...N 1.6%, Cl...H 15.0 %, O...H 21.4 %, C...H 16.5 %, and N...H 11.4%, and N...O 5.0%, and other interactions are less than 1.0%. Whereas enantiomer **4** is H...H 37.8 %, Cl...N 2.0%, Cl...H 12.6 %, O...H 15.1 %, C...H 13.7 %, and N...H 14.6%, and C...O 1.0%, and other interactions are less than 1.0%. The primary intermolecular interactions are observable in the fingerprint plot. This study gives the exact contribution of different types of interactions like C-H...O interaction contributes 21.4% & 15.1%, whereas CH- π interactions contribution is 16.5% & 13.7% for enantiomer **3** & **4** respectively.

The surface coverage for compound **5** is H...H 32.4 %, C...C 2.5%, N...H 14.6 %, O...H 18.3 %, C...H 11.4 %, O...O 8%, and H...Cl 7.2%, and C...Cl 5.8%, and other interactions are less than 1 %. The primary intermolecular interactions are observable in the fingerprint plot. This study gives the exact contribution of different types of interactions like $\pi-\pi$ interaction contributes 2.5%, whereas CH- π interactions contribution is 11.4%.

Calculated interaction energy with non-covalent interactions for enantiomer **3**, **4** & **5** are in supplementary table S4, S5 & S6 respectively. The Hirshfeld weak interactions calculation also supports the presence of weak non-covalent intermolecular interactions as in crystal packing, where C-H...N interactions, C-H...N, and C-H...O interactions of compound **3** & **4** in the crystal packing structure is in Figs. 13 & 14. The dispersion component and electrostatic forces calculated for these interactions are the dominating factors due to aromatic electronic redistribution in the compound and weak interactions in compound **3**, **4** & **5** [48]. In extensive hydrogen-bonding network of calculated interactions of compound **3** terminal carbonyl oxygen & pyridone oxygen are involved in weak inter-

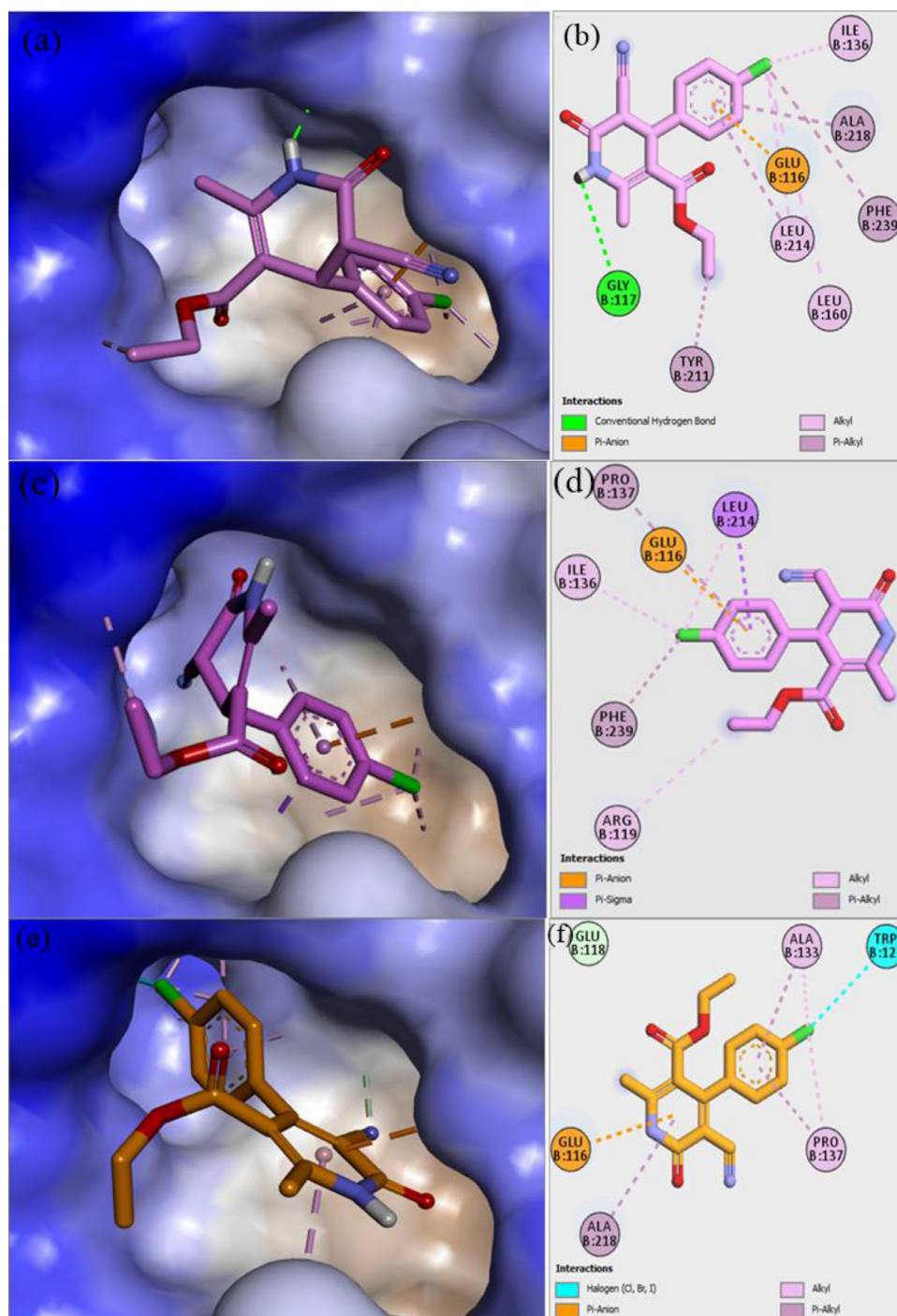


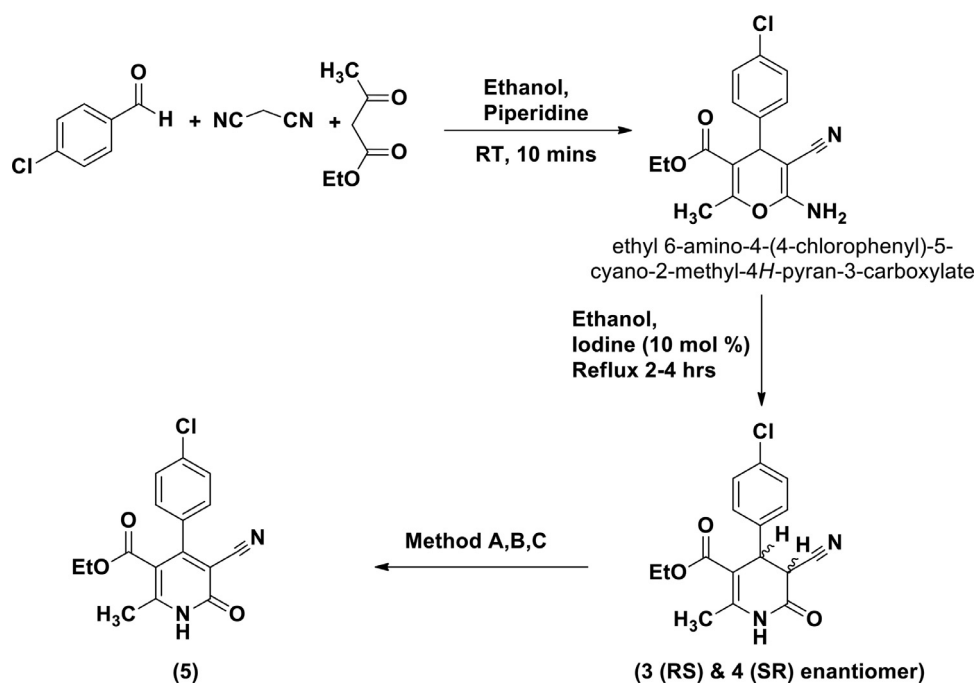
Fig. 20. Binding mode of compounds 3, 4, and 5 in the active site cavity of Eg5 protein and 2D represents their interactions. (a) & (b) Compound 3. (c) & (d) Compound 4. (e) & (f) Compound 5.

action and were forming 6, 8 & 12 membered R_2^1 (6), R_2^2 (8) & R_2^2 (12) ring in which C-H...O interactions are involved. In extensive hydrogen-bonding network of calculated interactions of compound 4 terminal carbonyl oxygen & pyridone, oxygen is involved in weak interaction and was forming 6, 12 & 20 membered R_2^1 (6), R_2^2 (12) & R_2^2 (20) ring in which C-H...O & C-H...N interactions are involved in a similar way as in a crystal.

In an extensive hydrogen-bonding network of calculated compound 5 terminal carbonyl oxygen & pyridone interactions, oxygen is involved in the weak interaction. It forms 6 & 14 membered R_2^1 (6) & R_2^2 (14) ring C-H...O interactions (Fig. 15). Different weak interactions stabilize both enantiomer 3 & 4 due to different

polarized structures. The dispersion component is the significant component in interaction energy, presumably a result of the aromatic electronic redistribution [49]. Another interaction of interest is weak H-bonds (C-H...O and C-H...N), making a non-covalent interaction among neighbor molecules. Electrostatic interaction is a significant component in C-H...O interactions. However, the dispersion component is a major one found in C-H...N interactions, presumably a result of the charge distribution in the ester functional group and cyano group and the polarization of the phenyl ring by its substituents.

The curvedness plots and the Shape index plots of 3D Hirshfeld also reveal the various weak intermolecular interactions in



Scheme 1. Synthesis of compound 3, 4 & 5. Method A: Ethanol, DDQ, MW 2 mins, method B: Ethanol, DDQ, Thermal 8-10 mins, method C: 1/202, RT.

compounds **3**, **4** & **5**. Yellow spots represent the crystal structure's weak interactions, shown in Fig. 16. The green-colored flat regions in the curvedness plots indicate weak π - π stacking in the crystal structure of compound **5** [49]. The red-yellow colored spots in curvedness plots show strong hydrogen-bonding interactions in the crystal structure.

Red and blue areas represent the acceptor and the donor property, respectively, in the shape index of compounds **3**, **4** & **5** (Fig. 17). Yellowish-red colored concave regions indicate the presence of weak intermolecular interactions in the Shape index plots [50,51]. The red and blue colored triangles on the surface of rings of the molecule in the Shape index plots also indicated the presence of weak π - π stacking in the crystal structure (Fig. 17). Hirshfeld surface analysis gives evidence about weak intermolecular interactions, and all these weak interactions stabilize and strengthen the crystal packing structure of compound **3**, **4** & **5**. Both enantiomers **3** & **4** show a relatively good difference in shape index and curvedness.

Molecular docking studies

The survivin protein has two discrete binding sites at the dimerization interface and the BIR domain. However, only the dimerization interface and the allosteric site near it have been reported to accommodate small molecules' binding [52–54]. The docking analysis has shown that compounds **3** and **4** occupy the region at the dimerization interface (Figs. 18a & 18b) with the binding affinities of -6.0 and -6.1 kcal/mol, respectively (Table 14). The dihydropyrimidone ring of compound **3** & **4** and the groups attached to it do not significantly interact with the residues at the dimerization interface. Moreover, both compounds **3** and **4** showed no hydrogen bond interactions, but they are stabilized at the interface by the hydrophobic π - π T-shaped, π -alkyl, and alkyl interactions (Figs. 18c & 18d). The lack of π interactions between the side chain residues and dihydropyrimidone ring of compounds **3** and **4** can be attributed primarily to the ring's non-aromaticity.

Although compounds **3** and **4** are stereoisomeric, their interface space occupation is different because their configuration at C-4 and

C-5 are different. The Chlorobenzene ring of compound **3** exhibited π - π T-shaped interaction with the residue Phe101 and π -alkyl interactions with the residues Leu6 and Leu98. It also exhibited alkyl interaction between the chlorine atom and the residue Leu98. Likewise, the stability of compound **4** is contributed significantly by π - π T-shaped interactions with the residues Phe101 and Phe93, π -alkyl interactions with the residue Phe101 and Leu98, and alkyl interactions with the residues Leu96, Leu98, Leu6, and Leu14.

In contrast to enantiomers **3** and **4**, the aromatic compound **5** (binding score -6.1 kcal/mol) interacts in the allosteric cavity near the dimerization interface and resembles the pose of compound **2** (reference compound) (Fig. 19). In the binding cavity, the residue Glu40 facilitates π -anion interaction and hydrogen bond interaction with the ring and N-H of dihydropyrimidone. It also exhibited π -alkyl interaction with the residue Lys90 and alkyl interactions with the residues Ile74 and Leu87.

The common trend in the binding interactions of compounds **3**, **4**, **5**, and **1** (monastrol) in the cavity of Eg5 is that the ester group protrudes outside the cavity. The π -interactions between the side chain residues and the dihydropyrimidine rings of compounds **3** and **4** were not observed again due to the ring's non-aromaticity. The chlorobenzene ring of compounds **3** and **4** is directed towards the hydrophobic region of the active site of Eg5 (Figs. 20a & 20c). However, the chlorobenzene ring of compound **5** favors the active site's hydrophilic region (Fig. 20e), which is assumed to be due to the halogen bond formation between the chlorine atom and the residue Trp127, where the same could not be formed in compounds **3** and **4**. The chlorobenzene ring of **3** and **4** are situated so that π -anion interactions with the negatively charged residue Glu116 will be favorable. Further, the residues Phe239, Leu214, Ala218, Ile136, Leu160, Tyr211, Leu214, and Pro137 facilitates the hydrophobic π -alkyl and alkyl interactions (Figs. 20b & 20d). Compound **5** adopted a conformation in which the aromatic ring of dihydropyrimidone established π -anion interactions with the residue Glu116, and the hydrophobic alkyl and π -alkyl interactions with the residues Ala218, Ala133, and Pro137 (Fig. 20f).

The results of this study indicated that the crystal compounds **3**, **4**, and **5** might induce apoptosis through inhibition of survivin

and Eg5 proteins, and thus it could be promising anticancer agents. The docking results also revealed that the aromaticity and planarity of rings played a crucial role in determining the position for interactions in the binding cavity. Although the enantiomers are stereoisomeric, the differences in their spatial arrangement of atoms could change the binding mode in the protein.

Conclusion

In the present work, the enantiomers **3**, **4** & **5** were synthesized and characterized using the FT-IR, ^1H & ^{13}C NMR, and single-crystal X-ray diffraction. The theoretical structures of **3**, **4** & **5** in both media were determined in the gas and aqueous solutions using the hybrid B3LYP/6-311 ++ G **method. The results have shown that dipole moment increases from the gas phase to solution with a slight contraction in the volume with significant solvation energy. All three types of charges evidenced that the protonation in solution could occur only in the amide nitrogen atom because these charges on these atoms show negative values. These charges predict that both O atoms could be protonated in solution. The mapped MEP surfaces show that the nucleophilic region is wide and is located on the Oxygen and Nitrogen atoms of the cyano group. At the same time, two explicit electrophilic sites are observed on the N-H bond of the ring. NBO calculations support the high stability of **3**, **4** & **5** in solution. The vibrational assignments of all vibration modes expected for **3**, **4** & **5** were reported together. Good correlations were obtained when the predicted ^1H and ^{13}C -NMR spectra are compared with the corresponding experimental ones for **3**, **4** & **5**. Based on docking studies using Survivin inhibitor and Kinesin Eg5 protein, the enantiomer **3**, **4** & **5** compounds can be studied to develop anticancer agents.

Declaration of Competing Interest

None.

Acknowledgments

The DBT and CSIR project supported this work. The authors are grateful to the Department of Chemistry, Mizoram University, Aizawl, Mizoram, India, and the DST-FIST to provide departmental facilities. Tezpur University and Gauhati University are acknowledged for single crystal X-ray crystallography (SCXRD) and IICT Hyderabad is acknowledged for NMR and HRMS data collection. Lalhruaizela acknowledges the CSIR for a senior research fellowship in the CSIR project. Brilliant N. Marak acknowledges the MoTA for NFAST research fellowship. Jayanta Dowaraha acknowledges the DST for Inspire fellowship.

Credit author statement

I am giving work contribution in “**Study of supramolecular self-assembly of pyridone and dihydropyridone co-crystal: Synthesis, crystal structure, Hirshfeld surface, DFT and molecular docking studies**” by all authors. Credits of all authors are as given:

1. Lalhruaizela: He has synthesized all the compounds.
2. Brilliant N. Marak: He has done all docking analysis and supplementary data preparation.
3. Dipanta Gogoi: He has done DFT calculations.
4. J. Dowaraha: He helped in synthesis, Hirshfeld calculation and crystallization.
5. Balkaran S. Sran: Single crystal data analysis.
6. Dr. Zodinpuia pachau: He helped in DFT calculation.
7. Dr. Ved Prakash Singh: Conceptualization, Methodology, Manuscript writing and all analysis.

Supplementary materials

Supplementary material associated with this article can be found, in the online version, at doi:[10.1016/j.molstruc.2021.130214](https://doi.org/10.1016/j.molstruc.2021.130214).

References

- [1] K. Rodrigues Rogerio, F. Vitorio, A. Eugen Kummerle, C.S. Graebin, Multi-component Reactions: A Brief History and their Versatility for the Synthesis of Biologically Active Molecules, *Rev. Virtual Quim* 8 (2016) 1934–1962, doi:[10.21577/1984-6835.20160132](https://doi.org/10.21577/1984-6835.20160132).
- [2] L.M. Ramos, B.C. Guido, C.C. Nobrega, J.R. Corrêa, R.G. Silva, H.C.B. de Oliveira, A.F. Gomes, F.C. Gozzo, B.A.D. Neto, The Biginelli Reaction with an Imidazolium-Tagged Recyclable Iron Catalyst: Kinetics, Mechanism, and Antitumor Activity, *Chem. Eur. J.* 19 (2013) 4156–4168, doi:[10.1002/chem.201204314](https://doi.org/10.1002/chem.201204314).
- [3] T.U. Mayer, Small Molecule Inhibitor of Mitotic Spindle Bipolarity Identified in a Phenotype-Based Screen, *Science* 286 (1999) 971–974, doi:[10.1126/science.286.5441.971](https://doi.org/10.1126/science.286.5441.971).
- [4] C.O. Kappe, Biologically active dihydropyrimidones of the Biginelli-type – a literature survey, *Eur. J. Med. Chem.* 35 (2000) 1043–1052, doi:[10.1016/S0223-5234\(00\)01189-2](https://doi.org/10.1016/S0223-5234(00)01189-2).
- [5] T.M. Kapoor, T.U. Mayer, M.L. Coughlin, T.J. Mitchison, Probing Spindle Assembly Mechanisms with Monastrol, a Small Molecule Inhibitor of the Mitotic Kinesin, Eg5, *Journal of Cell Biology* 150 (2000) 975–988, doi:[10.1083/jcb.150.5.975](https://doi.org/10.1083/jcb.150.5.975).
- [6] L. Duan, T.-Q. Wang, W. Bian, W. Liu, Y. Sun, B.-S. Yang, Centrin: Another target of monastrol, an inhibitor of mitotic spindle, *Spectrochim. Acta A* 137 (2015) 1086–1091, doi:[10.1016/j.saa.2014.08.050](https://doi.org/10.1016/j.saa.2014.08.050).
- [7] Y.A. Abassi, B. Xi, W. Zhang, P. Ye, S.L. Kirstein, M.R. Gaylord, S.C. Feinstein, X. Wang, X. Xu, Kinetic Cell-Based Morphological Screening: Prediction of Mechanism of Compound Action and Off-Target Effects, *Chem. Biol.* 16 (2009) 712–723, doi:[10.1016/j.chembiol.2009.05.011](https://doi.org/10.1016/j.chembiol.2009.05.011).
- [8] L. Zhu, P. Cheng, N. Lei, J. Yao, C. Sheng, C. Zhuang, W. Guo, W. Liu, Y. Zhang, G. Dong, S. Wang, Z. Miao, W. Zhang, Synthesis and Biological Evaluation of Novel Homocamptothecins Conjugating with Dihydropyrimidine Derivatives as Potent Topoisomerase I Inhibitors, *Arch. Pharm. Pharm. Med. Chem* 344 (2011) 726–734, doi:[10.1002/ardp.201000402](https://doi.org/10.1002/ardp.201000402).
- [9] G. Öztürk, D.D. Erol, T. Uzbay, M.D. Aytemir, Synthesis of 4(1H)-pyridinone derivatives and investigation of analgesic and antiinflammatory activities, *Il Farmaco* 56 (2001) 251–256, doi:[10.1016/S0014-827X](https://doi.org/10.1016/S0014-827X).
- [10] A. Abadi, O. Al-Deeb, A. Al-Afify, H. El-Kashef, Synthesis of 4-alkyl (aryl)-6-aryl-3-cyano-2(1H)-pyridinones and their 2-imino isosteres as nonsteroidal cardiotoxic agents, *Il Farmaco* 54 (1999) 195–201, doi:[10.1016/S0014-827X](https://doi.org/10.1016/S0014-827X).
- [11] M. Cocco, New bis(pyridyl)methane derivatives from 4-hydroxy-2-pyridones: synthesis and antitumoral activity, *Eur. J. Med. Chem* 38 (2003) 37–47, doi:[10.1016/S0223-5234](https://doi.org/10.1016/S0223-5234).
- [12] P. Storck, A.-M. Aubertin, D.S. Grierson, Tosylation/mesylation of 4-hydroxy-3-nitro-2-pyridinones as an activation step in the construction of dihydropyrido[3,4-b]benzo[f][1,4]thiazepin-1-one based anti-HIV agents, *Tetrahedron Lett.* 46 (2005) 2919–2922, doi:[10.1016/j.tetlet.2005.02.128](https://doi.org/10.1016/j.tetlet.2005.02.128).
- [13] J. Dowaraha, B.N. Marak, Lalhruaizela, B.S. Sran, V.P. Singh, Design, Synthesis, In Silico Analysis, and Structural Study of 4,6-Dimethyl-2-(3-(p-tolyloxy)propoxy)nicotinonitrile Fleximer, *Cryst. Res. Technol* (2020) 2000100, doi:[10.1002/crat.202000100](https://doi.org/10.1002/crat.202000100).
- [14] F.F. Fleming, L. Yao, P.C. Ravikumar, L. Funk, B.C. Shook, Nitrile-Containing Pharmaceuticals: Efficacious Roles of the Nitrile Pharmacophore, *J. Med. Chem.* 53 (2010) 7902–7917, doi:[10.1021/jm100762r](https://doi.org/10.1021/jm100762r).
- [15] J. Mirkovic, D. Mijin, S. Petrovic, Properties and synthesis of milrinone, *Hem Ind.* 67 (2013) 17–25, doi:[10.2298/HEMIND120410057M](https://doi.org/10.2298/HEMIND120410057M).
- [16] K. Shimizu, T. Murata, K. Okumura, V.C. Manganiello, T. Tagawa, Expression and role of phosphodiesterase 3 in human squamous cell carcinoma KB cells, *Anti-Cancer Drugs* 13 (2002) 875–880, doi:[10.1097/00001813-200209000-00014](https://doi.org/10.1097/00001813-200209000-00014).
- [17] I.W. Cheney, S. Yan, T. Appleby, H. Walker, T. Vo, N. Yao, R. Hamatake, Z. Hong, J.Z. Wu, Identification and structure–activity relationships of substituted pyridones as inhibitors of Pim-1 kinase, *Bioorg. Med. Chem. Lett.* 17 (2007) 1679–1683, doi:[10.1016/j.bmcl.2006.12.086](https://doi.org/10.1016/j.bmcl.2006.12.086).
- [18] N.A. Aquí, R.H. Vonderheide, Survivin as a universal tumor antigen for novel cancer immunotherapy: Functions of a killer clone, *Cancer Biol. Ther.* 7 (2008) 1888–1889, doi:[10.4161/cbt.7.12.7219](https://doi.org/10.4161/cbt.7.12.7219).
- [19] A.H. Abadi, D.A. Abouel-Ella, J. Lehmann, H.N. Tinsley, B.D. Gary, G.A. Piazza, M.A.O. Abdel-Fattah, Discovery of colon tumor cell growth inhibitory agents through a combinatorial approach, *Eur. J. Med. Chem.* 45 (2010) 90–97, doi:[10.1016/j.ejmech.2009.09.029](https://doi.org/10.1016/j.ejmech.2009.09.029).
- [20] C.-M.J. Hu, L. Zhang, Nanoparticle-based combination therapy toward overcoming drug resistance in cancer, *Biochem. Pharmacol* 83 (2012) 1104–1111, doi:[10.1016/j.bcp.2012.01.008](https://doi.org/10.1016/j.bcp.2012.01.008).
- [21] J.L. Markman, A. Rekechenetskiy, E. Holler, J.Y. Ljubimova, Nanomedicine therapeutic approaches to overcome cancer drug resistance, *Adv. Drug Deliv. Rev.* 65 (2013) 1866–1879, doi:[10.1016/j.addr.2013.09.019](https://doi.org/10.1016/j.addr.2013.09.019).
- [22] J. Kausteklis, V. Aleksa, M.A. Iramain, S.A. Brandán, Effect of cation-anion interactions on the structural and vibrational properties of 1-butyl-3-methyl imidazolium nitrate ionic liquid, *J. Mol. Struct.* 1164 (2018) 563–576, doi:[10.1016/j.molstruc.2018.03.100](https://doi.org/10.1016/j.molstruc.2018.03.100).

- [23] Y. Bouzian, K. Karrouchi, Y. Sert, C.-H. Lai, L. Mahi, N.H. Ahabchane, A. Talbaoui, J.T. Mague, E.M. Essassi, Synthesis, spectroscopic characterization, crystal structure, DFT, molecular docking and in vitro antibacterial potential of novel quinoline derivatives, *J. Mol. Struct.* 1209 (2020) 127940, doi:10.1016/j.molstruc.2020.127940.
- [24] O. Noureddine, S. Gatfaoui, S.A. Brandán, H. Marouani, N. Issaoui, Structural, docking and spectroscopic studies of a new piperazine derivative, 1-Phenylpiperazine-1,4-dium bis(hydrogen sulfate), *J. Mol. Struct.* 1202 (2020) 127351, doi:10.1016/j.molstruc.2019.127351.
- [25] S. Gatfaoui, N. Issaoui, S.A. Brandán, T. Roisnel, H. Marouani, Synthesis and characterization of p-xylylenediaminium bis(nitrate). Effects of the coordination modes of nitrate groups on their structural and vibrational properties, *J. Mol. Struct.* 1151 (2018) 152–168, doi:10.1016/j.molstruc.2017.09.027.
- [26] O. Noureddine, S. Gatfaoui, S.A. Brandán, A. Sagaama, H. Marouani, N. Issaoui, Experimental and DFT studies on the molecular structure, spectroscopic properties, and molecular docking of 4-phenylpiperazine-1-ium dihydrogen phosphate, *J. Mol. Struct.* 1207 (2020) 127762, doi:10.1016/j.molstruc.2020.127762.
- [27] BrukerSAINT, Version 6.36A, Bruker AXS Inc., Madison, Wisconsin, USA, 2001.
- [28] BrukerSADABS, Bruker AXS Inc., Madison, Wisconsin, USA, 2014.
- [29] G.M. Sheldrick, *SHELXT* – Integrated space-group and crystal-structure determination, *Acta Crystallogr. A* 71 (2015) 3–8, doi:10.1107/S2053273314026370.
- [30] G.M. Sheldrick, Crystal structure refinement with *SHELXL*, *Acta Crystallogr. C Struct. Chem* 71 (2015) 3–8, doi:10.1107/S2053229614024218.
- [31] O.V. Dolomanov, L.J. Bourhis, R.J. Gildea, J.A.K. Howard, H. Puschmann, *OLEX2*: a complete structure solution, refinement and analysis program, *J. Appl. Crystallogr.* 42 (2009) 339–341, doi:10.1107/S0021889808042726.
- [32] A.D. Becke, Density-functional exchange-energy approximation with correct asymptotic behavior, *Phys. Rev. A* 38 (1988) 3098–3100, doi:10.1103/PhysRevA.38.3098.
- [33] C. Lee, W. Yang, R.G. Parr, Development of the Colle-Salvetti correlation-energy formula into a functional of the electron density, *Phys. Rev. B* 37 (1988) 785–789, doi:10.1103/PhysRevB.37.785.
- [34] M.J. Frisch, G.W. Trucks, H.B. Schlegel, G.E. Scuseria, M.A. Robb, J.R. Cheeseman, G. Scalmani, V. Barone, G.A. Petersson, H. Nakatsuji, X. Li, M. Caricato, A.V. Marenich, J. Bloino, B.G. Janesko, R. Gomperts, B. Mennucci, H.P. Hratchian, J.V. Ortiz, A.F. Izmaylov, J.L. Sonnenberg, D. Williams-Young, F. Ding, F. Lipparini, F. Egidi, J. Goings, B. Peng, A. Petrone, T. Henderson, D. Ranasinghe, V.G. Zakrzewski, J. Gao, N. Rega, G. Zheng, W. Liang, M. Hada, M. Ehara, K. Toyota, R. Fukuda, J. Hasegawa, M. Ishida, T. Nakajima, Y. Honda, O. Kitao, H. Nakai, T. Vreven, K. Throssell, J.A. Montgomery Jr., J.E. Peralta, F. Ogliaro, M.J. Bearpark, J.J. Heyd, E.N. Brothers, K.N. Kudin, V.N. Staroverov, T.A. Keith, R. Kobayashi, J. Normand, K. Raghavachari, A.P. Rendell, J.C. Burant, S.S. Iyengar, J. Tomasi, M. Cossi, J.M. Millam, M. Klene, C. Adamo, R. Cammi, J.W. Ochterski, R.L. Martin, K. Morokuma, O. Farkas, J.B. Foresman, D.J. Fox, *Gaussian 16, Revision C.01*, Gaussian, Inc., Wallingford CT, 2016.
- [35] S. Miertuš, E. Scrocco, J. Tomasi, Electrostatic interaction of a solute with a continuum. A direct utilization of AB initio molecular potentials for the prediction of solvent effects, *Chemical Physics* 55 (1981) 117–129, doi:10.1016/0301-0104.
- [36] J. Tomasi, M. Persico, Molecular Interactions in Solution: An Overview of Methods Based on Continuous Distributions of the Solvent, *Chem. Rev.* 94 (1994) 2027–2094, doi:10.1021/cr00031a013.
- [37] A.V. Marenich, C.J. Cramer, D.G. Truhlar, Universal Solvation Model Based on Solute Electron Density and on a Continuum Model of the Solvent Defined by the Bulk Dielectric Constant and Atomic Surface Tensions, *J. Phys. Chem. B* 113 (2009) 6378–6396, doi:10.1021/jp810292n.
- [38] B.H. Besler, K.M. Merz, P.A. Kollman, Atomic charges derived from semiempirical methods, *J. Comput. Chem.* 11 (1990) 431–439, doi:10.1002/jcc.540110404.
- [39] E.D. Gledening, J.K. Badenhop, A.D. Reed, J.E. Carpenter, F.F. Weinhold, *NBO 3.1*, Theoretical Chemistry Institute, University of Wisconsin, Madison, WI, 1996.
- [40] GaussView, Version 6.1, Roy Dennington, Todd A. Keith, and John M. Millam, Semichem Inc., Shawnee Mission, KS, 2016.
- [41] R. Ditchfield, Self-consistent perturbation theory of diamagnetism: I. A gauge-invariant LCAO method for N.M.R. chemical shifts, *Mol. Phys.* 27 (1974) 789–807, doi:10.1080/00268977400100711.
- [42] K. Karrouchi, S.A. Brandán, Y. Sert, H. El-marzouqi, S. Radi, M. Ferbinteanu, M.E.A. Faouzi, Y. Garcia, M. Ansar, Synthesis, X-ray structure, vibrational spectroscopy, DFT, biological evaluation and molecular docking studies of (E)-N'-(4-(dimethylamino)benzylidene)-5-methyl-1H-pyrazole-3-carbohydrazide, *J. Mol. Struct.* 1219 (2020) 128541, doi:10.1016/j.molstruc.2020.128541.
- [43] M.J. Turner, J.J. McKinnon, S.K. Wolff, D.J. Grimwood, P.R. Spackman, D. Jayatilaka, M.A. Spackman, *CrystalExplorer17*, The University of Western Australia Perth, WA, Australia, 2017.
- [44] O. Trott, A.J. Olson, AutoDock Vina: Improving the speed and accuracy of docking with a new scoring function, efficient optimization, and multithreading, *J. Comput. Chem.* (2009), doi:10.1002/jcc.21334.
- [45] E.F. Pettersen, T.D. Goddard, C.C. Huang, G.S. Couch, D.M. Greenblatt, E.C. Meng, T.E. Ferrin, UCSF Chimera—A visualization system for exploratory research and analysis, *J. Comput. Chem.* 25 (2004) 1605–1612, doi:10.1002/jcc.20084.
- [46] J.J. McKinnon, M.A. Spackman, A.S. Mitchell, Novel tools for visualizing and exploring intermolecular interactions in molecular crystals, *Acta Crystallogr. B* 60 (2004) 627–668, doi:10.1107/S0108768104020300.
- [47] C.F. Mackenzie, P.R. Spackman, D. Jayatilaka, M.A. Spackman, CrystalExplorer model energies and energy frameworks: extension to metal coordination compounds, organic salts, solvates and open-shell systems, *IUCrJ* 4 (2017) 575–587, doi:10.1107/S205225251700848X.
- [48] V.P. Singh, J. Dowarah, B.N. Marak, A.K. Tewari, Design, synthesis, in silico analysis with PPAR- γ receptor and study of non-covalent interactions in unsymmetrical heterocyclic/phenyl fleximer, *J. Chin. Chem. Soc.* (2020), doi:10.1002/jccs.202000215.
- [49] V.P. Singh, J. Dowarah, Lalhruaizela, D.K. Geiger, Structural and Non-Covalent Interactions Study of 2-Pyridone Based Flexible Unsymmetrical Dimer, *Cryst. Res. Technol.* 55 (2020) 1900136, doi:10.1002/crat.201900136.
- [50] S. Shyamapada, M. Christoph, S. Mitra, Synthesis, Crystal structure, and Hirshfeld Surface Analysis of a New Mixed Ligand Copper(II) Complex, *ACS* 63 (2016) 129–137, doi:10.17344/acsi.2015.2024.
- [51] R.K. Mudsainyan, A.K. Jassal, M. Arora, S.K. Chawla, Synthesis, crystal structure determination of two-dimensional supramolecular co-ordination polymer of silver(I) with 1,2-Bis(phenylthio)ethane and its Hirshfeld surface analysis, *J. Chem. Sci.* 127 (2015) 849–856, doi:10.1007/s12039-015-0839-5.
- [52] M.D. Wendt, C. Sun, A. Kunzer, D. Sauer, K. Sarris, E. Hoff, L. Yu, D.G. Nettekheim, J. Chen, S. Jin, K.M. Comess, Y. Fan, S.N. Anderson, B. Isaac, E.T. Olejniczak, P.J. Hajduk, S.H. Rosenberg, S.W. Elmore, Discovery of a novel small molecule binding site of human survivin, *Bioorg. Med. Chem. Lett.* 17 (2007) 3122–3129, doi:10.1016/j.bmcl.2007.03.042.
- [53] A. Berezov, Z. Cai, J.A. Freudenberg, H. Zhang, X. Cheng, T. Thompson, R. Murali, M.I. Greene, Q. Wang, Disabling the mitotic spindle and tumor growth by targeting a cavity-induced allosteric site of survivin, *Oncogene* 31 (2012) 1938–1948, doi:10.1038/onc.2011.377.
- [54] T.M. Ibrahim, C. Ernst, A. Lange, S. Hennig, F.M. Boeckler, Small-Molecule Inter-vention At The Dimerization Interface Of Survivin By Novel Rigidized Scaffolds, *DDDT* 13 (2019) 4247–4263, doi:10.2147/DDDT.S224561.